

**Large nuclear scattering effects in antiproton transmission through polymer and metal-coated foils**K. Nordlund \**Department of Physics and Helsinki Institute of Physics, Faculty of Science, University of Helsinki, FI-00014 Helsinki, Finland*M. Hori *Max-Planck-Institut für Quantenoptik Hans-Kopfermann-Strasse 1, 85748 Garching, Germany  
and Fakultät für Physik, Ludwig-Maximilians-Universität München, 80799 Munich, Germany*

D. Sundholm

*Department of Chemistry, Faculty of Science, University of Helsinki, FI-00014 Helsinki, Finland*

(Received 18 March 2022; accepted 14 June 2022; published 6 July 2022)

We simulate the deceleration and transmission of antiprotons with keV-scale kinetic energies through polymer foils using a molecular dynamics approach, which includes a model of nuclear stopping based on the attractive interaction potentials between antiprotons and target atoms calculated by quantum chemical methods. Antiprotons scatter into larger angles with higher cross sections than protons. This causes a significant fraction of antiprotons to annihilate in the foil instead of emerging with energies of a few keV, especially when coatings of materials with high atomic number are applied to the surfaces. The simulation results are in good agreement with data from two experiments that involved pulsed antiproton beams with incident energies between 63 keV and 122 keV that traverse polymer foils with thicknesses of  $\approx 1.3 \mu\text{m}$  and  $1.8 \mu\text{m}$ . The 25-nm-thick layers of Ag on the latter foil reduced the transmission of antiprotons. The results will be utilized to design the degrader foils in laser spectroscopy experiments of antiprotonic helium atoms and experiments involving Penning traps that are carried out at the ELENA facility of CERN.

DOI: [10.1103/PhysRevA.106.012803](https://doi.org/10.1103/PhysRevA.106.012803)**I. INTRODUCTION**

The slowing down of ions with keV to MeV per nucleon kinetic energies in solids is conventionally described by the electronic  $S_e$  and nuclear  $S_n$  stopping powers [1–8]. The former corresponds to the deceleration of the ions by exciting or ionizing the electrons of the target atoms [4–7], whereas the latter arises from the elastic collisions of the ions with the atomic nuclei that are screened by the core electrons. The total stopping power is taken as the sum  $S = S_e + S_n$  [6–8], though changes in the interatomic forces caused by electronic excitation and ionization may give rise to couplings or synergetic effects between elastic and inelastic processes that cannot easily be handled by this simple separation [9–13]. While the electronic stopping powers of protons and antiprotons in materials are equal ( $S_e^p \approx S_e^{\bar{p}}$ ) at kinetic energies  $E_k$  above a few MeV, at lower velocities the proton value becomes greater ( $S_e^p > S_e^{\bar{p}}$ ) [14–40] which constitutes the Barkas effect [41,42]. The electronic stopping powers increase rapidly as the proton or antiproton slows down, eventually reaching maxima at around  $E_k = 100$  keV in many materials (see Fig. 1). At still lower energies the electronic stopping power decreases linearly with the particle velocity  $v$ , while the ratio  $R(v) \equiv S_e^{\bar{p}}/S_e^p$  decreases to  $\approx 0.5$  [20–23].

The nuclear stopping power  $S_n^{\bar{p}}$  of antiprotons, on the other hand, is difficult to measure because an elastic collision with a massive atom typically involves only a small reduction in the energy of the antiproton accompanied by a large scattering angle  $\theta$  that changes the direction of its movement [Figs. 2(a) and 2(b)]. The electronic stopping power including the contributions of ionization processes at low velocities have large theoretical and experimental uncertainties [29–37,43–45], and thus it is difficult to isolate the nuclear stopping power  $S_n^{\bar{p}}$  which is often assumed to be very small. Nevertheless it has been predicted that the  $S_n^{\bar{p}}$  contribution is larger than the value for protons and becomes an important energy-loss mechanism at  $E_k \leq 1$  keV (Fig. 1) [28,29,46–48]. Past theoretical [28–33,47] and experimental [46,49] studies of the nuclear stopping power have primarily concentrated on H, H<sub>2</sub>, or He gas targets.

Antiprotons arriving with small impact parameters relative to an atom follow complex trajectories that curve toward the nucleus with larger scattering angles  $\theta$  [see Fig. 2(a)] and cross sections [48] compared to protons that are deflected in the opposite direction along approximately hyperbolic trajectories in the repulsive proton-nucleus potential [28,29]. Similarly to the kinematics in elastic neutron moderation, the antiproton tends to lose the largest kinetic energy  $\Delta E$  per elastic collision with a target of similar mass, such as a hydrogen atom [Fig. 2(b)]. Collisions with heavier atoms involve larger cross sections and scattering angles, but lower  $\Delta E$  values that are kinematically allowed [48]. An experimental indication

\*kai.nordlund@helsinki.fi

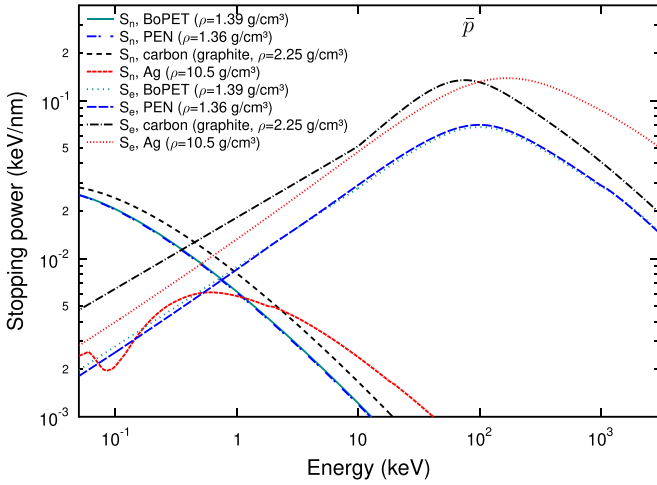


FIG. 1. Electronic  $S_e^{\bar{p}}$  and nuclear  $S_n^{\bar{p}}$  stopping powers of antiprotons in BoPET, PEN, C, and Ag targets used in the MD-RIA simulations. The nuclear stopping of Ag has structures at low energy due to the complicated trajectories in the attractive interatomic potential [48]. These  $S_n^{\bar{p}}$  values were calculated by integrating the energy transfer  $\Delta E$  (see Fig. 2) that was obtained by MD simulations of antiproton collisions with single atoms. At kinetic energies of a few hundred eV or less depending on the target atom or molecule, the cross section for an antiproton replacing one or more electrons and forming an antiprotonic atom are predicted to reach values of  $\text{\AA}^2$  scale [46,51–53]. This contribution is not included in this figure which is based on an adiabatic Born-Oppenheimer approximation that allows the separation of  $S_e^{\bar{p}}$  and  $S_n^{\bar{p}}$ .

of  $E_k = 1\text{--}10$  keV antiprotons reflecting off of an Al wall [50] has been interpreted in terms of consecutive Rutherford scatterings with multiple scattering angles between  $10^\circ$  and  $40^\circ$ . Depending on the target material, the deceleration process at energies of a few hundred eV or less include dominant contributions from some multi-electron and molecular effects that are less understood [45,51,52]. The antiproton eventually replaces one or more atomic electrons and forms an antiprotonic atom with  $\text{\AA}^2$ -scale cross sections [53–57]. The atom then undergoes electromagnetic cascade processes [58] which leads to the antiproton being absorbed into the nucleus and annihilating.

In-flight annihilation [59–73] constitutes a separate process in which an antiproton with keV-scale or higher energy encounters a nucleus and annihilates without forming an exotic atom. In the semiclassical black-disk model [66–69,74–76] which is believed to hold for target nuclei of large mass number  $A$  and an approaching antiproton of sufficiently short wavelength, the cross section of annihilation may be calculated as

$$\sigma_A = \pi R^2 \left( 1 + \frac{Ze^2(m_{\bar{p}} + M)}{4\pi\epsilon_0 E_k R M} \right). \quad (1)$$

Here the masses of the antiproton and nucleus are respectively denoted by  $m_{\bar{p}}$  and  $M$ , the vacuum permittivity by  $\epsilon_0$ , and the electric charge by  $e$ . The effective radius  $R$  is assumed to be largely independent of  $E_k$ . At energies below a few MeV, the Coulomb potential of the nucleus of charge number  $Z$  substantially curves the antiproton trajectory towards the nu-

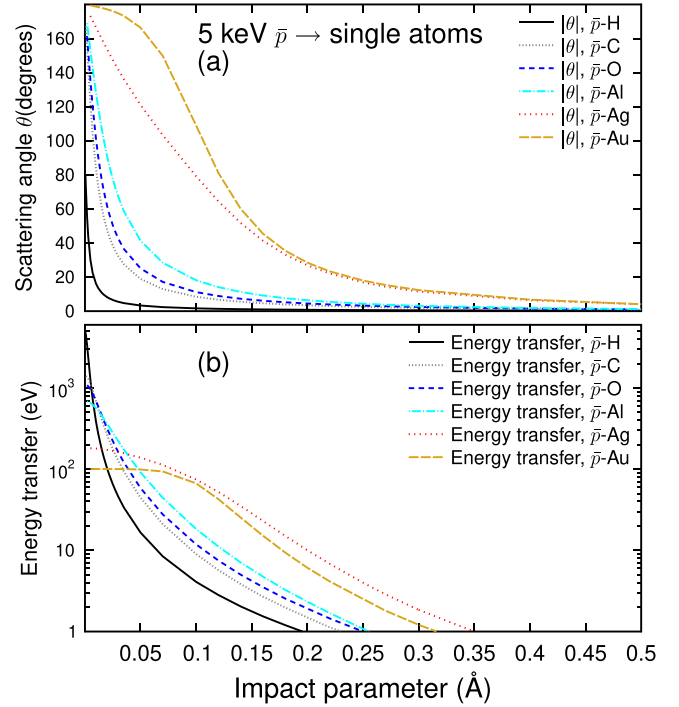


FIG. 2. (a) Scattering angle  $\theta$  and (b) kinetic energy transfer  $\Delta E$  in the laboratory frame of an elastic collision between an antiproton of incident energy  $E_k = 5$  keV and a H, C, O, Al, Ag, or Au atom as a function of the impact parameter  $b$ . The energy transfer for Ag and Au are kinematically limited to  $\Delta E = 100$  and  $200$  eV, respectively, by the reduced mass of the system and  $E_k$ . The values were obtained using MD simulations of collisions between an antiproton and each target atom that were based on the antiproton-atom potentials. The maximum impact parameters that lead to annihilation were  $b_A \approx 0.001$   $\text{\AA}$  and  $0.004$   $\text{\AA}$  for C and Au targets, respectively (see Fig. 6).

cleus so that the cross section increases and becomes roughly proportional to  $ZA^{1/3}$ .

We recently developed a molecular dynamics (MD) [77] approach in the Recoil Interaction Approximation (RIA) [78–80] to model the nuclear stopping powers for several atomic targets allowing simulations of the movement of keV antiprotons in solids [48,81]. The method is based on the interaction potential between antiprotons and atoms calculated by quantum chemical methods. This yielded a numerically intensive [82], but more precise way of simulating the effects of nuclear stopping and scattering on antiproton motion in solid targets.

In this work we show that the results of MD-RIA simulations are in good agreement with two sets of experimental data involving the transmission of antiprotons with incident energies between 63 keV and 122 keV through polymer foils, within the experimental uncertainties. The prolongation of the pathway of the antiprotons due to the nuclear scattering into large angles that naturally arises as part of our treatment of  $S_n^{\bar{p}}$  is found to significantly affect the transmission. Even a thin ( $\approx 25$ -nm-thick) layer of material with high atomic number such as Ag or Au deposited on the exit surface of the polymer foil was found to reduce the yield of the antiprotons emerging with energies of a few keV.

The Extra Low ENergy Antiproton (ELENA) storage ring [83,84] provides antiproton beams of 100 keV to several experiments that study antihydrogen [85–92], antiprotonic helium atoms ( $\bar{p}^4\text{He}^+ \equiv \bar{p} + {}^4\text{He}^{2+} + e^-$ ) [93–99], and the magnetic moment and cyclotron frequency of antiprotons confined in Penning traps [100–102]. Some of these experiments involve slowing down the antiprotons to energies  $E_{\text{trans}} \leq 5\text{--}10$  keV by allowing them to pass through foils of 1- $\mu\text{m}$ -scale thicknesses [90–92]. The antiprotons can then be efficiently captured in the electrostatic potential of a Penning trap of typical depth of  $5 \times 10$  kV. In other experiments the antiprotons are allowed to come to rest in gas targets of low density to form antiprotonic atoms in which the rates of collisions with the surrounding atoms are minimized. Such collisions may shift or broaden the measured spectral energies [103–107], cause the recapture of electrons by the antiprotonic atoms [108], or shorten the state lifetimes [58,109,110]. In some past experiments involving Penning traps, 5.3 MeV antiprotons provided by the Antiproton Decelerator (AD) [111–113] were slowed down in foils that were up to  $10^3$  times thicker. The stochastic nature of the straggling [23,114–116] in the electronic stopping due to the large number of collisions caused  $\approx 99.8\%$  of the antiprotons to annihilate in the foils before they could emerge at keV energies. The lower energy and momentum spread  $\Delta p/p \approx 10^{-3}$  of the ELENA beam are designed to reduce this loss of antiprotons [83,84]. This paper analyzes the effects of foil material and thickness on the antiproton deceleration and transmission.

The paper is organized in the following way. Two experiments that involve the slowing down of antiprotons in polymer foils, namely the laser spectroscopy experiment of  $\bar{p}^4\text{He}^+$  and some measurements using a Penning trap [91], are described in Secs. II A and II B, respectively. The models of nuclear and electronic stopping powers used in the simulations are outlined in Secs. III A and III B. Some details of the MD-RIA simulation are provided in Sec. III C. The transmission probabilities and energy distributions of the antiprotons emerging from the foils obtained from MD-RIA, GEANT4, and SRIM2013 simulations are compared with the experimental results in Sec. IV. The effects of various experimental conditions were included in the simulation in a stepwise manner. Some discussions and conclusions are provided in Sec. V.

## II. EXPERIMENTAL METHODS

### A. Laser spectroscopy of $\bar{p}^4\text{He}^+$

We utilized laser spectroscopy of  $\bar{p}^4\text{He}^+$  [95,96] to determine the relative numbers of antiprotons that were transmitted through a polyethylene naphthalate (PEN) foil of nominal thickness  $t_r = 1300$  nm. The foil acted as a hermetically sealed window of a cryogenic helium gas target and withstood a differential pressure of 100 Pa. PEN consists of H, C, and O atoms that causes less nuclear scattering during the transmission of the antiprotons compared to heavier atoms.

The three-body  $\bar{p}^4\text{He}^+$  atom consists of a helium nucleus, an electron in the  $1s$  state, and an antiproton occupying a Rydberg state with large principal and angular momentum quantum numbers  $n \approx \ell + 1 \approx 38$ . For this experiment the AD provided a  $\Delta t \approx 150$  ns long pulsed beam contain-

ing some  $(2\text{--}3) \times 10^7$  antiprotons of energy 5.3 MeV at a repetition rate of 0.008 Hz. The antiprotons entered a radiofrequency quadrupole decelerator (RFQD) [117–119] which contained four 3.4-m-long rod electrodes excited at a frequency of 202.6 MHz to produce a maximum electric field of 33 MV/m. A (20–25)% fraction of the antiprotons that matched the longitudinal acceptance of the device emerged with a nominal energy  $E_{\text{nom}} = 63$  keV, emittance of  $>50$   $\pi$  mm mrad, and 1 standard-deviation energy spread  $\sigma_E \approx 5$  keV. The remaining antiprotons either passed through the RFQD with incomplete deceleration or struck the RF electrodes and were not used. The average energy of the slow antiprotons was varied between  $E_{\text{nom}} - V_{\text{bias}} = 63$  keV and 122 keV by biasing the RFQD with a DC potential between  $V_{\text{bias}} = 0$  kV and  $-59$  kV. The antiprotons were then diverted by an achromatic momentum analyzer that was connected to the output of the RFQD, and focused into a  $d \approx 15$  mm-diameter spot at the entrance of a helium gas target. The spatial profiles of the beam at three locations along the beamline were measured by secondary electron emission detectors consisting of wire electrodes [120]. The relative intensity of the beam was measured by a lead fluoride Cherenkov detector [121].

The antiprotons traversed the PEN window and came to rest in a chamber filled with  ${}^4\text{He}$  gas having a pressure of  $\approx 100$  Pa and temperature  $T \approx 1.5$  K. This resulted in the formation of  $\bar{p}^4\text{He}^+$ . At a time  $t \approx 8$   $\mu\text{s}$  after the formation, a 40-ns-long laser pulse with a diameter of 50 mm and a pulse energy of 2 mJ was fired into the chamber in a counter-propagating direction to the antiproton beam [122]. The laser wavelength of 264.7 nm was tuned to excite a transition between a  $\bar{p}^4\text{He}^+$  resonance parent state  $(n, \ell) = (32, 31)$  with a 1  $\mu\text{s}$ -scale lifetime, and a daughter state  $(31, 30)$  that led to Auger emission of the electron with a lifetime of  $\approx 3$  ns. The  $\bar{p}^4\text{He}^{2+}$  ions that remained were destroyed by collisions with other helium atoms in the target [123,124]. The sharp increase in the flux of charged pions that emerged from the antiproton annihilations was detected by an acrylic Cherenkov detector [125]. The intensity of the signal was proportional to the number of atoms that were irradiated by the laser beam, and the population occupying the parent state  $(32, 31)$  corresponding to  $\approx 10^{-3}$  of the number of antiprotons that came to rest in the helium gas [58]. The signal indicating the transmission of antiprotons through the foil was measured as a function of the beam energy.

These measurements were repeated using eight foils of the same nominal thickness over a period of 8 years [95,96], and the reproducibility of the  $E_k$  dependence was found to be distributed over  $\pm 5$  keV in terms of incident energy. The average thicknesses of two of the foils were measured using a Rutherford backscattering technique [69,126] and found to be within  $\pm 10\%$  of the nominal values which roughly agrees with the values reported by other authors [127]. Prior to the measurements, the foils were evacuated to a pressure of between  $10^{-6}$  Pa and  $10^{-7}$  Pa at room temperature for several days to reduce the contamination on their surfaces. The foils were then cooled to  $T \leq 1.5$  K and the spectroscopy experiments were carried out. Thin layers of contamination gradually froze on the foil surfaces over time so that the transmission of the

antiprotons was affected. The contamination was removed by heating the foil to room temperature.

### B. Antiproton Penning trap

The second set of experimental results were obtained using a Penning trap [90] as reported in Ref. [91]. We here describe the experimental details that are relevant for the comparison with the simulations. The beam emerging from the RFQD entered the bore of a superconducting solenoidal magnet of field  $B = 2.5$  T. The antiprotons traversed a pair of biaxially oriented polyethylene terephthalate (BoPET) foils with nominal thickness  $t_r = 900$  nm which constituted the position-sensitive cathodes of a beam profile monitor, before being captured within the cylindrical electrodes of the trap with a total length of  $\approx 700$  mm and an inner diameter of 40 mm. A  $(25 \pm 3)$ -nm-thick layer of Ag was deposited on the front surface of each BoPET foil by vacuum evaporation. Patterns of ten 0.94-mm-wide electrode strips with a 1 mm pitch between neighboring strips were then fabricated on the Ag surfaces using a laser trimmer [120,128]. The pair of patterned foils were stacked with the two Ag electrode surfaces that provided the horizontal and vertical projections of the beam facing outwards. The material layers were thus arranged in the sequence Ag, BoPET, and Ag with thicknesses  $t_r = 25$  nm, 1800 nm, and 25 nm, respectively. Antiprotons traversing the electrodes induced secondary electron emission. By measuring the corresponding charge signal induced on each electrode strip with a charge-sensitive preamplifier, a full-width-at-half-maximum beam diameter of 2–3 mm was observed [91].

The relative intensity of annihilations in the foils at beam energies between  $E_k = 92$  keV and 122 keV was measured by a Cherenkov detector [125] which was placed outside the solenoidal magnet. In a separate measurement, antiprotons of average incident energy  $E_k = 111.5$  keV traversed the foils and traveled along the axis of the solenoid, before reaching a plate located  $l > 1.5$  m away outside the magnetic bore. By scanning the electrostatic potential applied to an electrode of the trap and measuring the relative intensity of the annihilations on the plate, the energy distribution  $E_{\text{trans}}$  of the antiprotons that emerged from the foil were determined. The Ag coatings developed pinholes over several years [129] which may alter the transmission properties.

## III. SIMULATION METHOD

### A. Nuclear stopping model

#### 1. Simulation models of nuclear stopping

In many models of nuclear stopping, the trajectory of each ion in the target is tracked to simulate the effects of nuclear scattering which alter the direction of the ion movement. In the binary collision approximation (BCA) [8,130,131] the pathway of the positively charged ion is separated into a series of isolated two-body collisions with the target atoms. The ion follows a hyperbolic trajectory in the repulsive potential of the atom, but BCA employs computationally efficient methods to determine the straight ion pathway that is asymptotic to the actual hyperbola for each collision [131,132]. The electronic stopping  $S_e$  contribution slows down the ion in the straight

pathways between the collisions. The SRIM2013 code [8,133] utilizes the Monte Carlo variant of BCA, in which after each collision the impact parameter  $b$  relative to the next target atom is stochastically chosen according to a probability distribution. SRIM2013 does not, however, allow the simulation of antiprotons since the code is based on calculating the asymptotes of hyperbolic trajectories [132], whereas negatively charged particles that are deflected inwards toward the nucleus within an attractive potential follow more complicated trajectories [48].

The GEANT4 code [134] has been used to simulate the passage of MeV to GeV antiprotons through materials for many years. The cumulative effects of a large number of collisions and scatterings into small angles that occur within an ion trajectory segment of given length are here approximated by one of several multiple scattering models that may be selected by the user [135–140]. The computations involved in these so-called “condensed” simulations are vastly reduced compared to the MD method that explicitly solves the equations of motion for every collision that the ion undergoes (see below). We used the Wentzel-VI multiple scattering model [135,138–141] implemented in GEANT4 version 10.7 to simulate the antiproton scatterings into smaller angles. The code separately calculated the contributions of nuclear scattering events into larger angles by using a single elastic scattering model. This model was based on the Wentzel scattering function [135,142] with the same shape as the one used in the above multiple scattering model. The electronic stopping power  $S_e^{\bar{p}}$  of antiprotons was modeled by treating the atoms as an ensemble of quantum harmonic oscillators [15,39,143–145].

MD-RIA by comparison models ions and atoms moving under arbitrary interatomic forces [77,146,147]. This allows antiproton scatterings that occur in the attractive antiproton-atom potentials of multiple atoms comprising the lattice to be explicitly and more precisely simulated [48,78–81]. The MD [77,148] method follows the atomic motion over time in short ( $\lesssim 0.1$  Å) spatial steps in an iterative and deterministic way by calculating the sum of all the forces exerted from the neighboring atoms. The contributions of multiple simultaneous collisions that can increase the energy transfer  $\Delta E$  compared to the results of BCA at ion energies of  $\lesssim 1$  keV are thus inherently included. The method does not rely on any assumption regarding the specific scattering model, trajectory shape, or collision strength. In the recoil interaction approximation, only the interactions between the projectile ion and target atoms are evaluated, whereas the interactions between the lattice atoms that would vastly increase the computational time are neglected [78].

#### 2. Interaction potentials

We calculated the interaction potentials between antiprotons and Cu, Ag, and Au atoms that include the contributions of atomic screening functions using the method of Ref. [48]. Density functional theory (DFT) calculations provided the interaction energy between the antiproton (treated as a negative point charge surrounded by the basis functions of the hydrogen atom) and a Cu, Ag, or Au nucleus surrounded by its 29, 47, or 79 electrons, respectively. The interaction energy as a function of the distance between the atomic nucleus

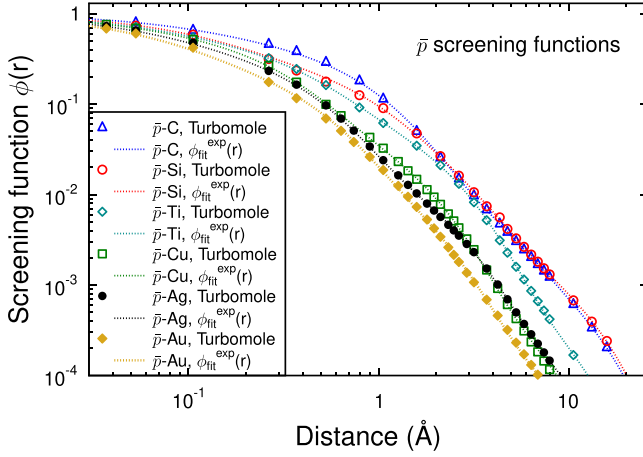


FIG. 3. The results of the best fit of the screening function  $\phi_{\text{fit}}^{\text{exp}}(r)$  of Eq. (3) on the interaction potentials between an antiproton and C, Si, Ti, Cu, Ag, or Au atom. The C, Si, and Ti functions are reproduced from Ref. [48].

and the antiproton was calculated at 48 discrete points in the range between  $r = 0.0001$  bohr and 50 bohr using version 7.5 of the Turbomole code [149–151]. The calculations were performed at the DFT level with the range-separated  $\omega$ B97X-D functional in the meta-generalized gradient approximation (mGGA) using grid 7, which is a dense integration grid [152,153]. The Cu atomic orbitals were expanded in a decontracted triple- $\zeta$  polarization (def2-TZVP) basis set, whereas for the antiproton a decontracted hydrogen def2-TZVP basis set was utilized [154]. For the Ag atom, a decontracted Turbomole all-electron TZVP basis set (TZVPPalls2) was used. For the Au atom, we used the relativistic exact two-component (X2C) Hamiltonian and the decontracted x2c-TZVPPall Au basis set [155,156]. The corresponding level of theory was used in the nonrelativistic calculations on Au. These interaction energies are provided in the Appendix.

The calculated data were fit to a Coulomb potential with an exponential screening term of the form

$$V(r) = \frac{1}{4\pi\epsilon_0} \frac{Z_1 Z_2 e^2}{r} \phi(r). \quad (2)$$

Here  $Z_1 = -1$ ,  $Z_2$ , and  $e$  denote the antiproton, nuclear, and elemental charges, respectively. The screening term  $\phi(r)$  was taken to have the exponential form [48]

$$\phi_{\text{fit}}^{\text{exp}}(r) = b_1 e^{a_1 r} + b_2 e^{a_2 r} + b_3 e^{a_3 r} + b_4 e^{a_4 r}. \quad (3)$$

TABLE I. The values of the coefficients  $b_i$  and  $a_i$  of the antiproton screening function  $\phi_{\text{fit}}^{\text{exp}}(r)$  of Eq. (3) that were obtained by the best fit to the calculated potentials between an antiproton and a Si, Cu, Ag, or Au atom. The coefficient of the last term is defined as  $b_4 \equiv 1 - b_1 - b_2 - b_3$  to ensure that the potential is of a pure Coulomb form with bare nuclear charges at short length scales  $r \rightarrow 0$ . The parameters for Si are obtained from Ref. [48].

Target	$b_1$	$b_2$	$b_3$	$a_1$	$a_2$	$a_3$	$a_4$
Si	0.00547494	0.360324	0.091372	-0.19811	-1.99426	-0.79267	-9.71705
Cu	0.00176877	0.715859	0.106417	-0.333232	-5.1509	-1.28497	-27.2726
Ag	0.000985221	0.563975	0.0374024	-0.260267	-3.91193	-0.944955	-19.0258
Au	0.000854978	0.400538	0.0380799	-0.322095	-3.86192	-1.21461	-17.2175

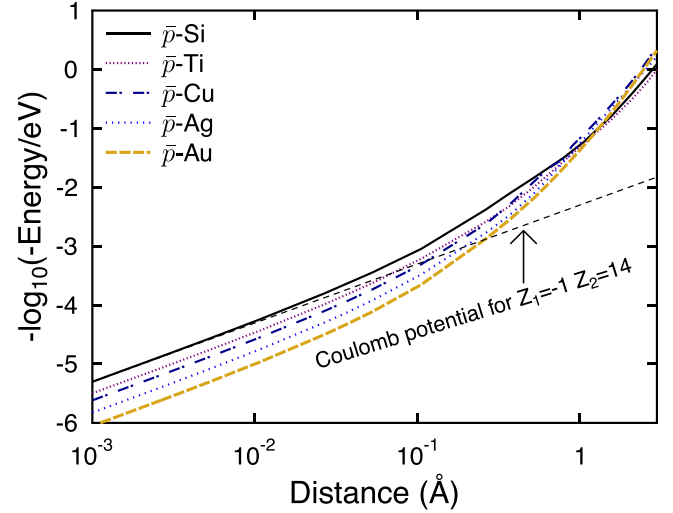


FIG. 4. Interaction potentials between an antiproton and target Si, Ti, Cu, Ag, and Au atoms calculated by quantum chemical methods. The Si and Ti potentials are reproduced from Ref. [48]. The bare Coulomb potential between an antiproton and Si atom is also shown for comparison.

The coefficient of the last term is defined as  $b_4 \equiv 1 - b_1 - b_2 - b_3$ , which ensures that the potential of Eq. (2) has a pure Coulomb form at short distances, i.e.,  $\phi_{\text{fit}}^{\text{exp}}(r \rightarrow 0) = 1$ . Figure 3 shows the calculated screening functions of the Cu, Ag, and Au atoms, together with those of C, Si, and Ti obtained previously [48]. The parameters  $b_i$  and  $a_i$  determined by the best fit of Eq. (3) to the calculated antiproton-Si, -Cu, -Ag, and -Au interaction potentials are summarized in Table I. The potentials involving Si, Ti, Cu, Ag, and Au atoms are shown in Fig. 4.

In Figs. 2(a) and 2(b), the scattering angle  $\theta$  and energy transfer  $\Delta E$  for an elastic collision between an antiproton of incident energy  $E_k = 5$  keV and a single isolated H, C, O, Al, Ag, or Au atom in the above potentials are shown as a function of impact parameter  $b$ . The results were obtained using a MD simulation of binary collisions between an antiproton and a single atom. The trajectories with impact parameters of less than  $b_A \approx 0.001$  Å and 0.004 Å for the C and Au targets, respectively, approach within a few femtometers of the nucleus [69,76,157]. These trajectories were removed from Figs. 2(a) and 2(b) based on a simplified approximation (labeled as model B in Sec. III A 4) of the effects of antiproton annihilations.

### 3. Nuclear stopping curve

The nuclear stopping powers  $S_n^{\bar{p}}$  of antiprotons in atomic C, H, O and Ag targets were calculated by integrating the energy transfer  $\Delta E$  over the impact parameter  $b$ . The Bragg averaging rule [1,8] was then applied to the results to obtain the  $S_n^{\bar{p}}$  values in the PEN and BoPET foils. These were found to be approximately equal (Fig. 1) and slightly smaller than the values for a pure C target of graphite density. As the antiprotons slow down from an energy of 10 keV to less than 1 keV, the  $S_n^{\bar{p}}$  values increase from  $\approx 1$  eV/nm to more than 10 eV/nm, eventually becoming larger than the electronic stopping powers which decrease from  $S_e^{\bar{p}} \approx 30$  eV/nm to less than 10 eV/nm over the same energy range. The nuclear stopping power of Ag is larger than those of the polymeric materials at energies above a few keV. As the antiproton slows down, the  $\Delta E$  value becomes kinematically limited so that a saturation at  $S_n^{\bar{p}} \approx 5$  keV/nm is seen.

### 4. Antiproton annihilation

The atoms in our MD-RIA simulations were fixed to the electronic ground states throughout the collisions. The contributions of some complex electronic processes that occur at energies of a few hundred eV or less, such as the antiproton replacing the atomic electrons and forming antiprotonic atoms [51–57] or effects involving electronically excited or ionized states of the target atom are therefore not included.

In most of the simulations, we instead modeled the nuclear absorption of antiprotons using a simplified and computationally efficient approach, henceforth called annihilation model A. The kinetic energy of the antiproton is evaluated throughout the collision with multiple atoms and during the deceleration due to the electronic stopping power. When this energy becomes smaller than the absolute value of the local interaction potential  $|\phi(r)|$ , the antiproton is taken to orbit the nucleus and annihilate. Though in-flight annihilation that occurs at higher energies are ignored, this model is sufficient to evaluate the fraction of the antiprotons transmitted through the foils.

In some of the MD-RIA simulations a more complex model B that takes both the in-flight annihilations and the capture of low-energy antiprotons into account was used. In this model annihilation occurs when the antiproton comes within the effective interaction radius  $r_A$  of the nucleus which is taken to be independent of the incident energy  $E_k$ . This black disk model is believed to be valid for massive target nuclei with diameters that are sufficiently large compared to the wavelength of the antiproton [66,74,76]. We used the average interaction radius

$$\langle r_A \rangle = 1.840 + 1.120(A)^{1/3} \text{ fm} \quad (4)$$

that was derived from the unified optical potential model of Ref. [76]. Equation (4) was obtained by folding the optical potential of the antiproton-proton system that was obtained from experiments carried out at  $E_k \approx 750$  keV, with the matter density distributions of the nuclei. Comparisons with the results of x-ray spectroscopy experiments of antiprotonic atoms with mass number  $A > 10$  have shown that the model reproduces

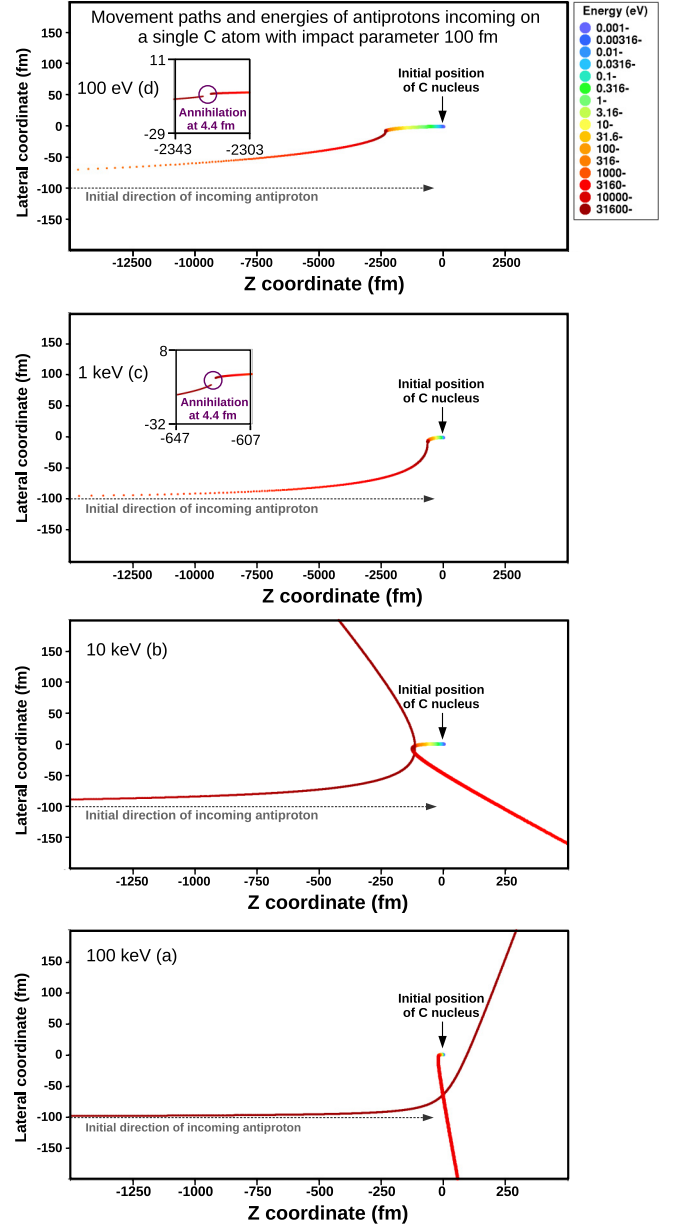


FIG. 5. Trajectory of an antiproton with an impact parameter  $b = 100$  fm and incident energy  $E_k = 100$  keV (a), 10 keV (b), 1 keV (c), or 100 eV (d) scattering off a single C atom positioned at the origin calculated by MD-RIA. Note the different horizontal and vertical scales. The gradients indicate the kinetic energies of the antiproton and C atom in logarithmic scale. Annihilations occur when the antiproton comes within  $\langle r_A \rangle = 4.4$  fm of the C atom [76] (see inserts). As the antiproton accelerates when approaching the nucleus, the integration steps in time are reduced to ensure the numerical stability of the results [78].

the shifts and widths of the atomic energy levels that arise due to the strong interaction [76]. These spectroscopy measurements effectively study the antiproton-nuclei scattering at nearly zero energy.

The simulated trajectories of antiprotons with impact parameter  $b = 100$  fm and incident energies  $E_k = 100$  keV and 10 keV that scatter off C atoms are shown in Figs. 5(a) and

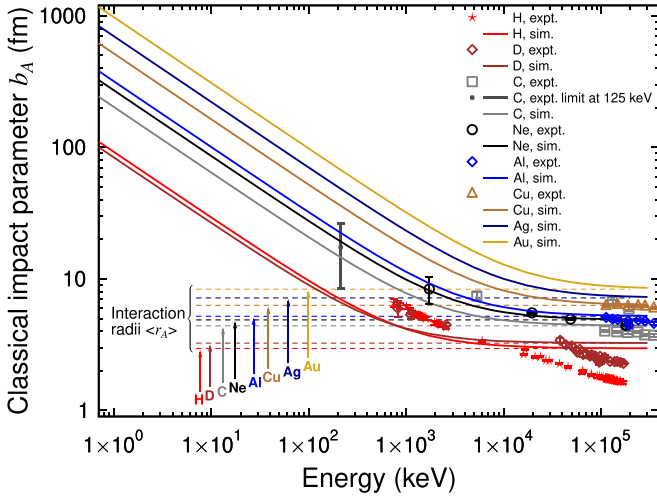


FIG. 6. Minimum impact parameter  $b_A$  of an antiproton colliding with a H, D, C, Ne, Al, Cu, Ag, or Au atom that leads to in-flight annihilation as a function of the incident energy  $E_k$  calculated using MD-RIA. The simulations utilized the average interaction radii  $\langle r_A \rangle$  according to Eq. (4) [76] shown in the figure for each target. The experimental values of H [59–62], D [63–65], C [68,70], Ne [71,72], Al, and Cu [70,73] targets that were obtained from the measured annihilation cross sections  $\sigma_A$  and assuming the relation  $\sigma_A = \pi b_A^2$  are shown superimposed. The vertical line with error bars for C at  $E_k = 125$  keV represents the experimental limit of Ref. [69]. The curves are arranged in the same sequence as in the indicated labels.

5(b), respectively. At lower energies  $E_k = 1$  keV [Fig. 5(c)] and 100 eV [Fig. 5(d)], the more pronounced curvature of the trajectories allow the antiprotons to approach the nuclei within the  $\langle r_A \rangle = 4.4$  fm distance implied by Eq. (4) and annihilate.

Figure 6 shows the values of the maximum impact parameter  $b_A$  that leads to annihilation in H, D, C, Ne, Al,

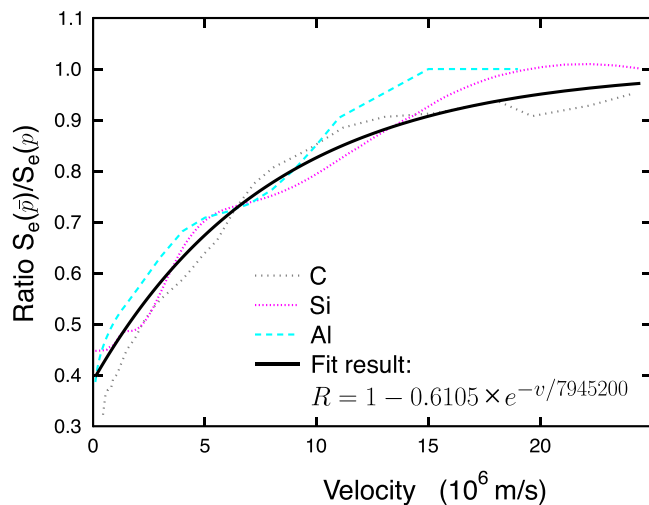


FIG. 7. The generalized electronic stopping ratio  $R(v)$  as a function of the velocity of the antiproton and proton. The dashed curves indicate the ratios  $S_e^{\bar{p}}/S_e^p$  between the experimental antiproton [20] and proton stopping powers in C, Si, and Al targets [20]. The solid curve shows the result of the best fit of the indicated exponential function.

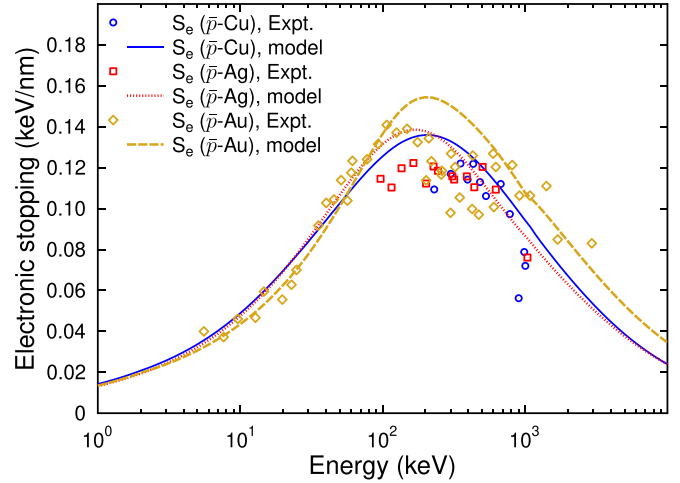


FIG. 8. Electronic stopping powers  $S_e^{\bar{p}}$  of antiprotons in Cu, Ag, and Au targets obtained from the generalized scaling method, compared with experimental data [20,21].

Cu, Ag, and Au nuclei that were determined in this way. Antiprotons of high energy ( $E_k \gtrsim 5$  MeV) approach the nuclei along straight trajectories so that the impact parameter  $b_A$  is roughly equal to  $\langle r_A \rangle$ . At lower energies, the focusing effect of the Coulomb force causes  $b_A$  to rapidly increase. The results were compared with the experimental cross section  $\sigma_A$  of antiproton annihilations which were taken to relate to the impact parameter as  $\sigma_A = \pi b_A^2$ . The lack of experimental data at energies below a few MeV makes this comparison difficult, but the simulation and experimental results are consistent for C [68–70], Ne [71,72], Al, and Cu [70,73] targets within the experimental uncertainties. Deviations are seen in H [59–62] and D [63–65] for which the semiclassical parametrization of Eq. (4) is not expected to be a good approximation. Indeed, partial-wave decomposition analysis [158,159] have shown that the cross sections for these light nuclei at low energies are dominated by the contributions of the  $s$ - and  $p$ -wave components of the approaching antiproton. The fraction of  $E_k = 1$ –100 keV antiprotons that undergo in-flight annihilation is relatively small (see below), as the corresponding  $b_A$  values of approximately 10–1000 fm are 2–4 orders of magnitude smaller than the interatomic distances of  $\approx 100$  pm.

## B. Electronic stopping

We developed a generalized expression for the electronic stopping power  $S_e^{\bar{p}}(v)$  of antiprotons to deduce the values in atomic targets for which experimental data were not available. The procedure was based on our observations (see Fig. 7) that the generalized stopping ratio  $R(v) \equiv S_e^{\bar{p}}(v)/S_e^p(v)$  between the experimental antiproton and proton stopping powers in C, Si, and Al targets [20] are equal over a range of antiproton velocities  $v$  within the experimental uncertainties. This is because the  $S_e$  values at low projectile velocities are approximately proportional to the electron density in the target [160,161]. We used the exponential parametrization,

$$S_e^{\bar{p}}(v) = R(v)S_e^p(v) = (1 - R_g e^{-v/v_g})S_e^p(v), \quad (5)$$

TABLE II. The results of MD-RIA simulations for an antiproton beam with an incident energy of 111.5 keV and energy spread of 5 keV traversing an uncoated BoPET foil, or foils with 25-nm-thick Al, Cu, Ag, or Au coatings with the indicated densities and total thickness of 1850 nm. The average path length  $R_{\text{path}}$ , electronic energy deposition  $F_{D_e}$ , fraction of antiprotons  $f_{\text{stop}}$  that come to rest in the foil, and average energy ( $E_{\text{trans}}$ ) of the emerging antiprotons are shown. Also indicated are the results for the Ag coating applied to only the entrance (labeled as upstream) or exit (downstream) foil surfaces, and with a hypothetical material Ag\* in which the electronic stopping power of Ag is adjusted to be equal to that of BoPET. The models A or B used to simulate the in-flight annihilation and low-energy capture of the antiprotons by the nuclei are indicated. The indicated uncertainties arise from the dispersion of the trajectories.

Coating material	Coated surface	Coating density ( $\text{g} \cdot \text{cm}^{-3}$ )	$R_{\text{path}}$ (nm)	$F_{D_e}$ (keV)	$f_{\text{stop}}$ (%)	$\langle E_{\text{trans}} \rangle$ (keV)	Annih. model
Uncoated			$1859 \pm 1$	$103.8 \pm 0.3$	$12.6 \pm 0.3$	$7.55 \pm 0.02$	A
Al	Both	2.7	$1855 \pm 1$	$104.3 \pm 0.5$	$16.5 \pm 0.5$	$7.21 \pm 0.04$	A
Cu	Both	9.0	$1844 \pm 1$	$105.5 \pm 0.5$	$33.8 \pm 0.7$	$6.76 \pm 0.04$	A
Ag	Both	10.5	$1840 \pm 1$	$105.8 \pm 0.4$	$39.0 \pm 0.4$	$6.69 \pm 0.02$	A
Ag	Both	10.5	$1834 \pm 4$	$106.1 \pm 0.2$	$35.7 \pm 2.1$	$6.48 \pm 0.12$	B, $\langle r_A \rangle = 4.4 \text{ fm}$
Ag	Both	10.5	$1840 \pm 1$	$106.0 \pm 0.1$	$39.0 \pm 0.4$	$6.69 \pm 0.02$	B, $\langle r_A \rangle = 10 \text{ fm}$
Ag	Upstream only	10.5	$1861 \pm 1$	$104.5 \pm 0.1$	$17.2 \pm 0.5$	$6.88 \pm 0.03$	A
Ag	Downstream only	10.5	$1839 \pm 1$	$105.1 \pm 0.1$	$32.1 \pm 0.6$	$7.33 \pm 0.04$	A
Ag*	Both	10.5	$1844 \pm 1$	$104.7 \pm 0.1$	$32.3 \pm 0.6$	$7.66 \pm 0.04$	A
Au	Both	19.3	$1830 \pm 2$	$106.3 \pm 0.7$	$53.7 \pm 0.9$	$6.68 \pm 0.05$	A

to reflect the experimental fact that at high velocities the electronic stopping powers of protons and antiprotons become approximately equal, i.e.,  $R(v \rightarrow \infty) = 1$ . The best fit on the experimental data for C, Al, and Si targets yielded values of  $R_g = 0.6105 \pm 0.013$  and  $v_g = (7.95 \pm 0.62) \times 10^6 \text{ m/s}$  for the two constants. The largest systematic deviations (Fig. 7) in the experimental data sets used in the fitting were  $-6\%$  for the C data, and  $7\%$  for Al. As the antiproton-atom interactions that are involved in the nuclear scattering do not follow a simple scaling relation relative to the proton-atom interactions, a similar scaling procedure could not be employed to deduce the nuclear stopping powers  $S_n^p$ .

Figure 8 compares the electronic stopping powers of antiprotons in Cu, Ag, and Au targets that were estimated using the scaling procedure of Eq. (5) with the experimental data [20,21]. The agreement is particularly good for the Au target at energies between  $E_k \approx 7 \text{ keV}$  and  $100 \text{ keV}$ , which indicates that the model is valid over a wide range of atomic targets. At higher energy regions deviations of up to  $15\%$  that are comparable with the fluctuations in the experimental data are seen. These electronic stopping powers together with those of BoPET, PEN, graphite, and Ag targets shown in Fig. 1 were used in the MD-RIA simulations.

### C. Simulation setup

The MD-RIA code MDRANGE [78,162] was used to simulate the transmission of antiprotons through a homogeneous PEN ( $\text{C}_{14}\text{H}_{10}\text{O}_4$ ) foil of thickness  $t_r = 1300 \text{ nm}$ , or three sequential layers of Ag, BoPET ( $\text{C}_{10}\text{H}_8\text{O}_4$ ), and Ag with  $t_r = 25 \text{ nm}$ ,  $1800 \text{ nm}$ , and  $25 \text{ nm}$ , respectively, that were utilized in the experiments. Simulations were also carried out for foils with Al, Cu, or Au coatings of the same thicknesses. The PEN and BoPET materials were modeled as  $2 \times 2 \times 2 \text{ nm}^3$  cubes containing atoms with the above elemental ratios and densities of  $1.36 \text{ g/cm}^3$  and  $1.38 \text{ g/cm}^3$ , respectively. As the materials lack any long-range order, the atoms were distributed at randomized locations with a minimum interatomic distance of  $1.1 \text{ \AA}$ . The evaporated

coatings were modeled as amorphous structures with the densities shown in Table II, as they were nanocrystalline with random surface orientations. As the channeling effects of keV antiprotons even in single crystals are predicted to be small [48], the simulation results were not significantly affected by the small cell size or the partial order in the polymeric materials. We included the electronic stopping power  $S_e^p(v)$  and straggling [114–116] in each foil layer. Past simulations of the transmission of  $E_k = 4 \text{ keV}$  protons through C foils have found that the straggling must be included to obtain a good agreement with experimental data [163].

The antiprotons arrived in a perpendicular direction to the foil surface with an energy spread that was taken to be Gaussian with a standard deviation  $\sigma_E = 5 \text{ keV}$  to simulate the properties of the RFQD beam. The initial lateral positions of the antiprotons were randomized over a  $1 \times 1 \text{ nm}^2$  area at the center of the  $2 \times 2 \times 2 \text{ nm}^3$  cubic cell to ensure an uniform sampling over different trajectories through the compound materials [48]. A few thousand random numbers that defined the initial positions and energies of the antiprotons were generated using the Mersenne twister [164] with a repeat period of  $2^{19937} - 1$ . The positions of the atoms were randomly shifted to simulate the thermal motion [165], but this had a negligible effect on the results for these amorphous materials. Between  $10^3$  and  $10^5$  trajectories were simulated to determine the energies and angles of the antiprotons that traversed the foil for each condition. The contributions of the nuclear stopping and scattering were isolated by comparing the results with other simulations (indicated as “ $S_e$  only” in the figures) in which the interparticle potential and forces were set to zero so that the slowing down was only due to the electronic stopping.

## IV. RESULTS

### A. Fractions of transmitted antiprotons

#### 1. Comparison with experiments

Figure 9(a) presents the relative intensity of the antiproton beam that traversed and emerged from the  $1300\text{-nm}$ -thick

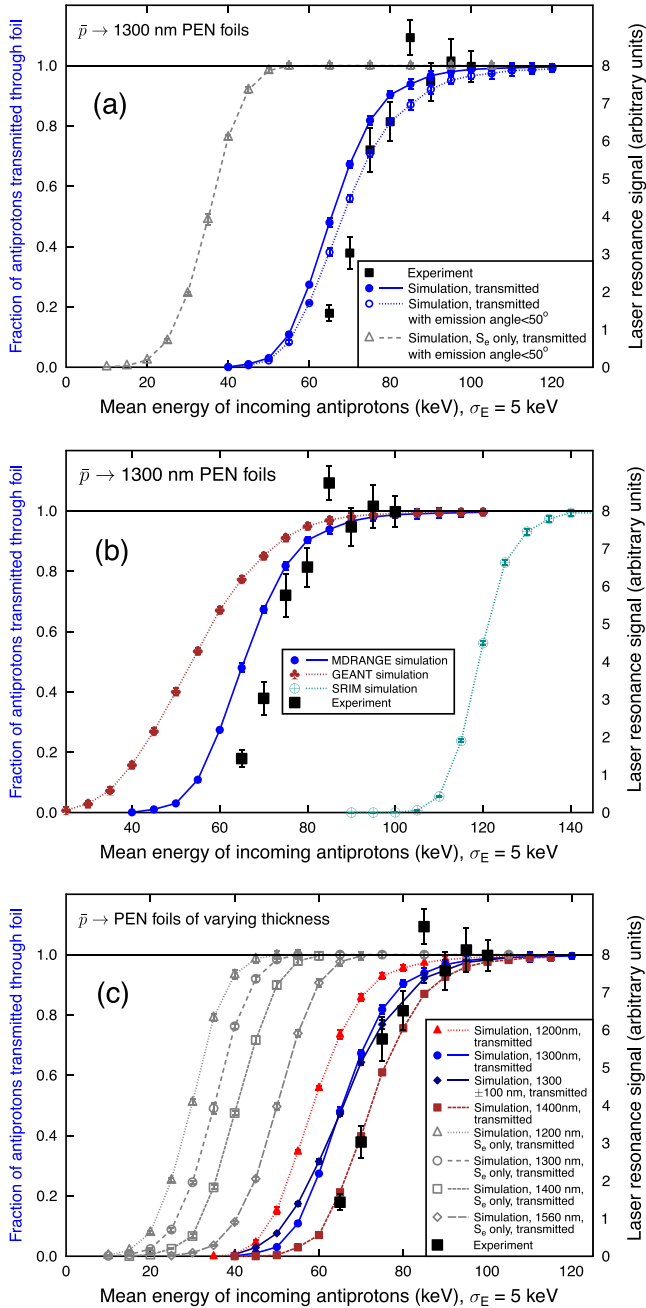


FIG. 9. (a) Relative intensities (filled squares) of antiprotons transmitted through a 1300-nm-thick PEN foil measured by laser spectroscopy of  $\bar{p}^4\text{He}^+$  as a function of the incident beam energy. The results of MD-RIA simulations with (filled circles) and without (open triangles) the nuclear scattering and stopping  $S_n$ , and the curve obtained by selecting the antiprotons that exit the foil with an angle  $\theta_{\text{exit}} < 50^\circ$  (open circles) are shown superimposed. (b) Simulation results for antiprotons of the MDRANGE and GEANT4 codes, and the proton result of SRIM2013. (c) Fractions of antiprotons that emerged from PEN foils of uniform thicknesses  $t_r = 1200$  nm, 1300 nm, 1400 nm, and 1560 nm simulated with and without the  $S_n^{\bar{p}}$  contribution. The results of a simulation in which the foil thickness was varied around the average value of 1300 nm by a standard deviation  $\sigma_t = 100$  nm are also shown.

PEN foil as a function of the incident energy  $E_k$  (indicated by filled squares), which was measured by laser spectroscopy of  $\bar{p}^4\text{He}^+$  [95,96]. Only the antiprotons that came to rest in the volume of the helium gas irradiated by the laser beam contributed to the signal. The results are therefore expected to be relatively insensitive to the trajectories of the antiprotons that exited the foil. A good agreement between the experimental and MD-RIA results (blue solid curve) is seen within the systematic uncertainties of the foil thickness (see below). The curve calculated by removing the nuclear stopping contribution is shifted to lower energies by 30 keV compared to the experimental data. Antiprotons that exited with a large off-normal angle  $\theta_{\text{exit}}$  may stop outside the area irradiated by the laser beam and avoid detection. We took this possible effect into account by rejecting the simulated antiprotons with  $\theta_{\text{exit}} > 50^\circ$ . This slightly improved the overall agreement between the simulation (blue dotted curve) and experimental results.

Figure 10(a) shows the results of the Penning trap experiment in which the fraction of antiprotons that annihilated in the Ag-coated BoPET foil or in its vicinity instead of being transmitted, was measured as a function of the beam energy. A good agreement with the MD-RIA results (blue solid curve) is seen except at the highest energy  $E_k = 122$  keV. The reason for this difference is not understood. Our simulations did not include the effects of the uniform magnetic field of  $B = 2.5$  T that was applied in the direction normal to the foil surface [91]. In the experiment, on the other hand, the antiprotons that emerged with a lateral velocity component  $v_\perp$  perpendicular to the normal of the foil surface underwent cyclotron motion with an approximate Larmor radius,

$$r_{\text{Larmor}} = \frac{m_{\bar{p}} v_\perp}{eB}. \quad (6)$$

Antiprotons with large radii eventually struck the inner walls of the trap or other electrodes that were located at the exit end of the solenoidal magnet [91]. The simulation results (blue dotted curve) obtained by assuming that the antiprotons with  $r_{\text{Larmor}} > 5$  mm annihilated and contributed to the signal is in better agreement with the experimental result at  $E_k = 122$  keV. When the effects of nuclear stopping and scattering  $S_n^{\bar{p}}$  are removed, the simulation results (gray dotted curve) shift to lower energies by a factor of 1.5–2 in terms of  $E_k$ .

The results of the GEANT4 simulation [Fig. 9(b)] for  $E_k < 80$  keV overestimate the transmission probability through the 1300-nm-thick PEN foil compared to the experimental data. A relatively good agreement is seen in the case of the  $E_k \geq 100$  keV antiprotons traversing the Ag-coated BoPET foil [Fig. 10(b)]. These simulations did not include the discrimination involving the Larmor radius and exit angle.

As SRIM2013 cannot handle antiprotons we used it to calculate the transmission of protons. The results [see Figs. 9(b) and 10(b)] were nearly identical to those of MDRANGE. Proton energies that are a factor 1.5–1.7 greater than for antiprotons are needed to traverse the foils because of the larger electronic stopping power.

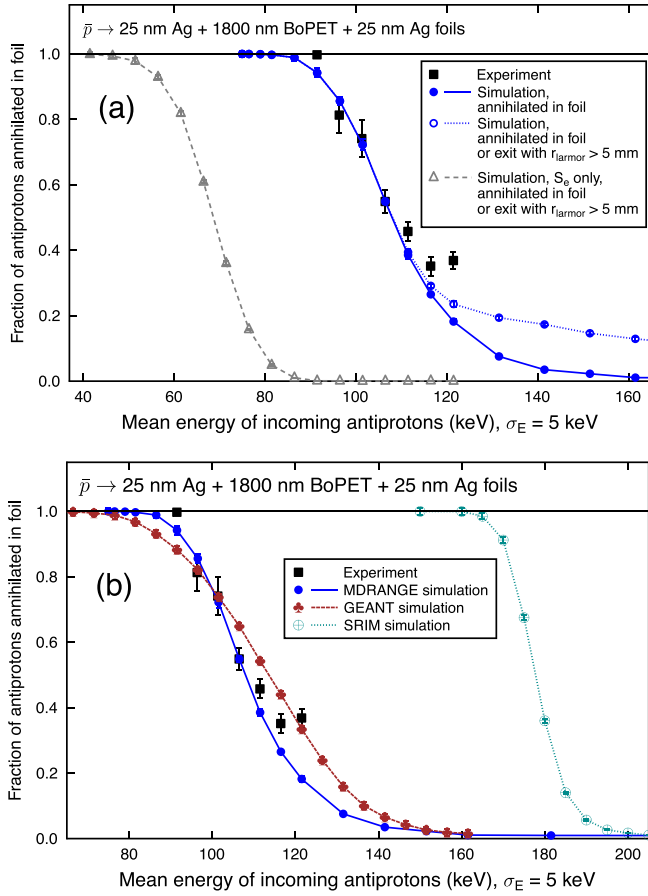


FIG. 10. (a) Experimental fractions of antiprotons (filled squares) [91] that annihilated in the BoPET foil instead of being transmitted, as a function of the incident energy  $E_k$ . The results of simulations with (filled circles) and without (open triangles) the nuclear stopping  $S_n^{\bar{p}}$  contribution, and by assuming that the antiprotons that exited the foil with a Larmor radius  $r_{Larmor} > 5$  mm rapidly annihilate (open circles). (b) Comparisons with MDRANGE and GEANT4 simulation results for antiprotons, and the proton result of SRIM2013.

## 2. Effects of foil thickness variation

The transmission probabilities of the antiprotons through PEN foils of uniform thicknesses  $t_r = 1200$  nm, 1300 nm, 1400 nm, and 1560 nm that were calculated with and without the nuclear stopping  $S_n^{\bar{p}}$  contribution are compared in Fig. 9(c). A change of  $\pm 100$  nm in  $t_r$  was found to shift the transmission probability curves by  $\pm(5-7)$  keV in terms of the incident beam energy  $E_k$ . The curve corresponding to  $t_r = 1400$  nm best agrees with the experiment. We next introduced random variations in the thickness across the foil surface which corresponded to a standard deviation  $\sigma_t = 100$  nm around the nominal value  $t_r = 1300$  nm. Similar thickness or equivalent density variations in BoPET foils have been reported by other authors [127]. The variation slightly flattened the shape of the transmission probability curve.

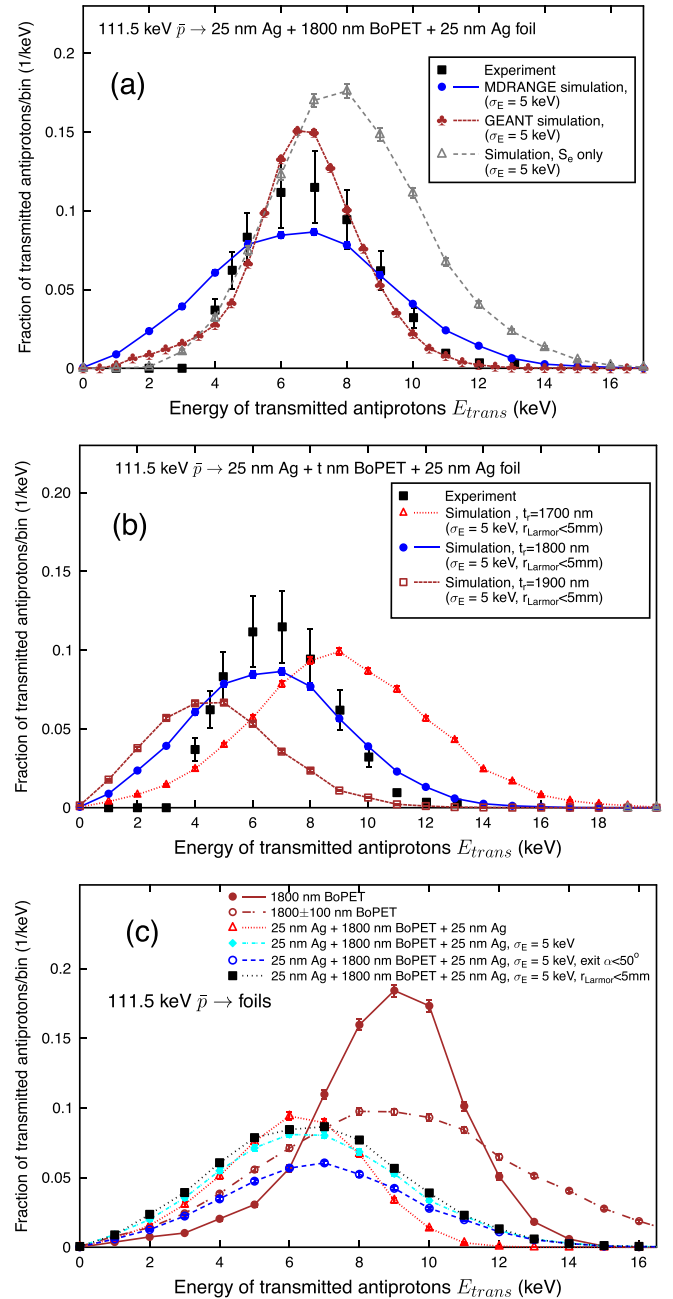


FIG. 11. (a) Experimental (filled squares) energy  $E_{trans}$  distributions of antiprotons that emerge from the 1800-nm-thick BoPET foil with Ag coatings [91] for an incident beam energy of 111.5 keV. The distribution is normalized to the fraction of antiproton annihilations according to Fig. 10. Simulated distributions calculated using MD-RIA with (filled circles) and without (open triangles) the contribution of nuclear stopping, normalized to the total number of incident antiprotons. The results of the GEANT4 code are shown superimposed. (b) Simulated distributions for foils of  $t_r = 1700$  nm (open red triangles), 1800 nm (filled circles), or 1900 nm (open squares) with Ag coatings. (c) The distributions for 1800-nm-thick foils with and without Ag coatings, and with a variation of the BoPET thickness  $\sigma_t = 100$  nm. The distributions obtained by selecting the antiprotons that exit the foil with an angle  $\theta_{exit} < 50^\circ$  or Larmor radius  $r_{Larmor} < 5$  mm are shown superimposed.

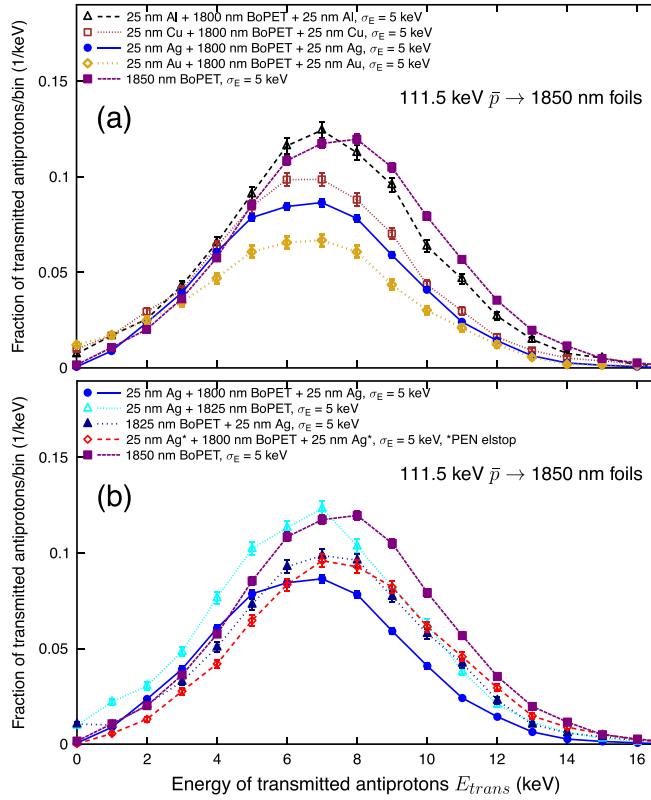


FIG. 12. (a) Simulated energy distributions of antiprotons emerging from a 1850-nm-thick uncoated BoPET foil, or foils with 25-nm-thick Al, Cu, Ag, or Au coatings applied on both sides. The incident beam energy was adjusted to 111.5 keV with a spread of 5 keV. (b) Distributions calculated for foils with 25-nm-thick Ag coatings applied to the entrance, exit, or both surfaces. The hypothetical case in which the electronic stopping power of Ag is adjusted to be equal to that of BoPET is indicated as Ag\*.

## B. Energy distributions of transmitted antiprotons

### 1. Comparisons with MD-RIA, GEANT4, and experiments

Figure 11(a) presents the measured and simulated energy distributions  $E_{\text{trans}}$  of antiprotons emerging from the 1800-nm-thick BoPET foil with Ag coatings used in the Penning trap experiment, for an average beam energy of 111.5 keV and energy spread of 5 keV [91]. The simulation results are normalized to the total number of incident antiprotons including those that stop in the foil, whereas the experimental data are normalized using the measured fractions of antiprotons that annihilated in or near the foil as shown in Fig. 10(a). The agreement between the MD-RIA and experimental results improves when the effects of nuclear stopping  $S_n^{\bar{p}}$  are included. The experiment detected few antiprotons of  $E_{\text{trans}} \leq 3$  keV. This may partially be due to the slow antiprotons that followed complex trajectories in the magnetic field and annihilated in the solenoidal magnet without being detected. Preliminary measurements at ELENA using a different apparatus and beam energy appear to show significant fractions of  $E_{\text{trans}} \approx 1$  keV antiprotons.

The energy distribution obtained from the GEANT4 code is in relatively good agreement with the experimental data within the systematic uncertainties. It is

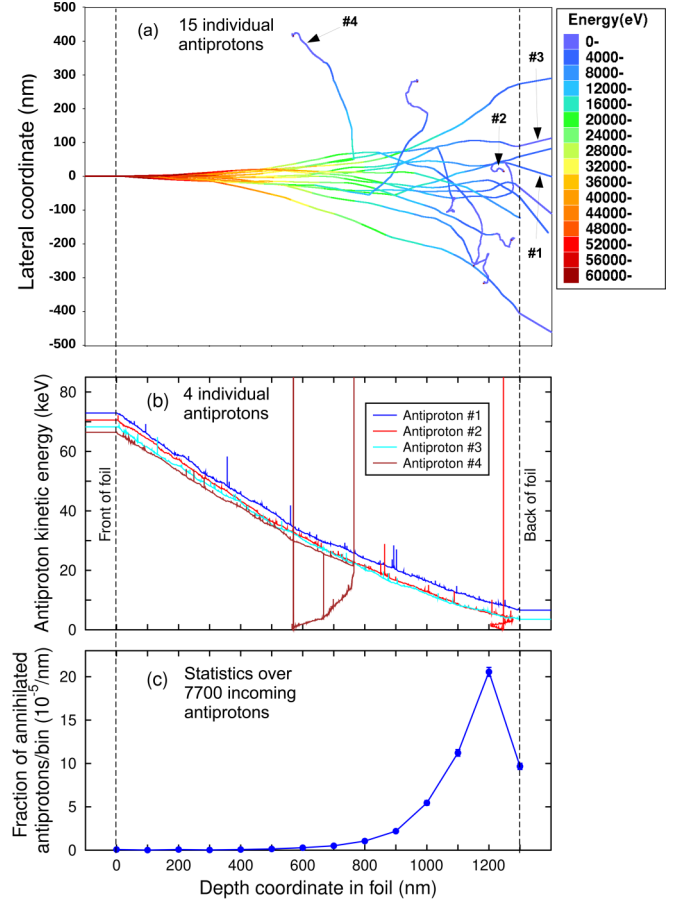


FIG. 13. (a) Trajectories of 15 antiprotons of incident energy 65 keV and energy spread 5 keV that traverse a 1300-nm-thick PEN foil calculated by MD-RIA. Color gradients indicate the antiproton energy, with the highest energy being on the left side of the figure and the lowest energy being on the right. Each trajectory begins at positions that are slightly laterally shifted. Some 40% of the antiprotons travel through and emerge from the foil. (b) Evolution of the energies of four antiprotons labeled #1–#4 in (a) projected along the depth coordinate of the foil, with #2 and #4 coming to rest in the foil. The peaks in the energy correspond to antiprotons being attracted by a nucleus during a close collision. (c) Spatial distribution of the antiproton annihilations projected along the depth coordinate.

peaked more sharply compared to the distribution obtained from MD-RIA.

### 2. Effects of thickness variation

The energy  $E_{\text{trans}}$  distributions of the antiprotons traversing BoPET foils of thicknesses  $t_r = 1700$  nm, 1800 nm, and 1900 nm with 25-nm-thick Ag coatings are compared in Fig. 11(b). Antiprotons with Larmor radii  $r_{\text{Larmor}} > 5$  mm were rejected. The curve for the nominal value  $t_r = 1800$  nm best agrees with the experimental results. An uncertainty of  $\pm 100$  nm on  $t_r$  was found to correspond to a  $\pm 3$  keV shift in the peak of the  $E_{\text{trans}}$  distribution. This shift is significant compared to the 5–10 kV confining electrostatic potential of the Penning trap, implying that a stack of foils having a thickness adjusted with an accuracy of  $\pm 50$  nm may be needed to trap the maximum number of antiprotons. Alternatively

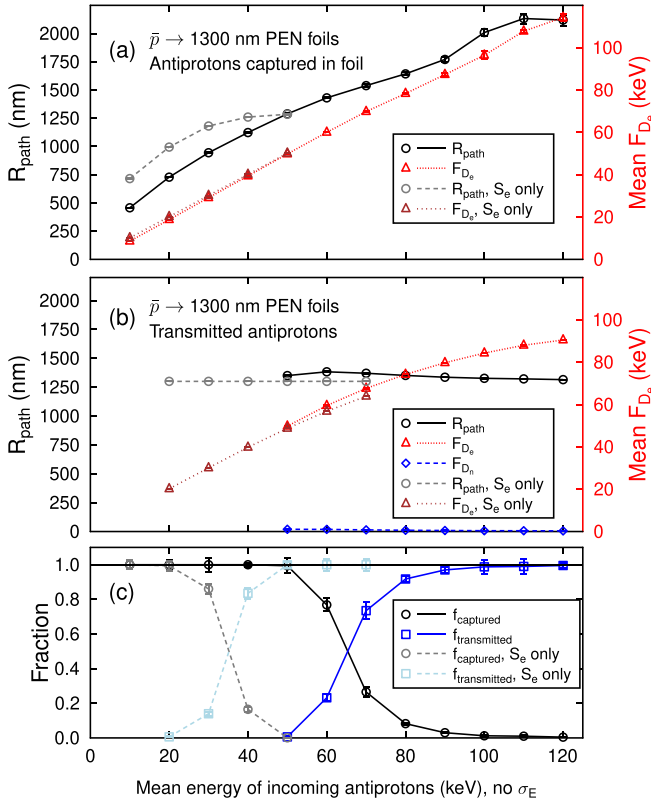


FIG. 14. Path lengths  $R_{\text{path}}$ , and total deposited electronic  $F_{D_e}$  and nuclear  $F_{D_n}$  energies of the cohort of antiprotons that (a) came to rest in, or (b) were transmitted through, a 1300-nm-thick PEN foil as a function of incident beam energy  $E_k$ . (c) The probabilities of the antiprotons being transmitted through the foil (indicated as  $f_{\text{transmitted}}$ ) or coming to rest in the foil ( $f_{\text{captured}}$ ). The curves calculated without the contribution of the nuclear stopping power are indicated as “ $S_e$  only.” The simulations were carried out for a monoenergetic beam.

the beam energy  $E_k$  may be tuned over a range of  $\pm 10$  keV to compensate for the typical uncertainty in the average foil thickness of  $\pm 100$  nm.

The distribution for a monoenergetic ( $\sigma_E = 0$ ) beam traversing a 1800-nm-thick BoPET foil is indicated by filled brown circles in Fig. 11(c). A foil with a typical thickness variation  $\sigma_t = 100$  nm across its surface (brown open circles) resulted in a reduction in the antiproton yield at the peak of the distribution located at  $\approx 9$  keV by factor of  $\approx 2$ , and a broadening of its width by several keV. The variation must be reduced to  $\sigma_t < 20\text{--}30$  nm to avoid this loss in the number of trapped antiprotons.

### 3. Effects of metallic coatings

When 25-nm-thick Ag coatings were applied to the two sides of the BoPET foil, the antiproton yield at the peak of the  $E_{\text{trans}}$  distribution [indicated using red open triangles in Fig. 11(c)] decreased by a factor of  $\approx 2$  and its position shifted from 9 keV to 6 keV compared to the above case of a monoenergetic beam traversing a bare uniform foil. The inclusion of an energy spread  $\sigma_E = 5$  keV in the beam further broadened the distribution (blue filled circles) towards higher energies by  $\approx 1$  keV. Rejecting the transmitted antiprotons with exit angles

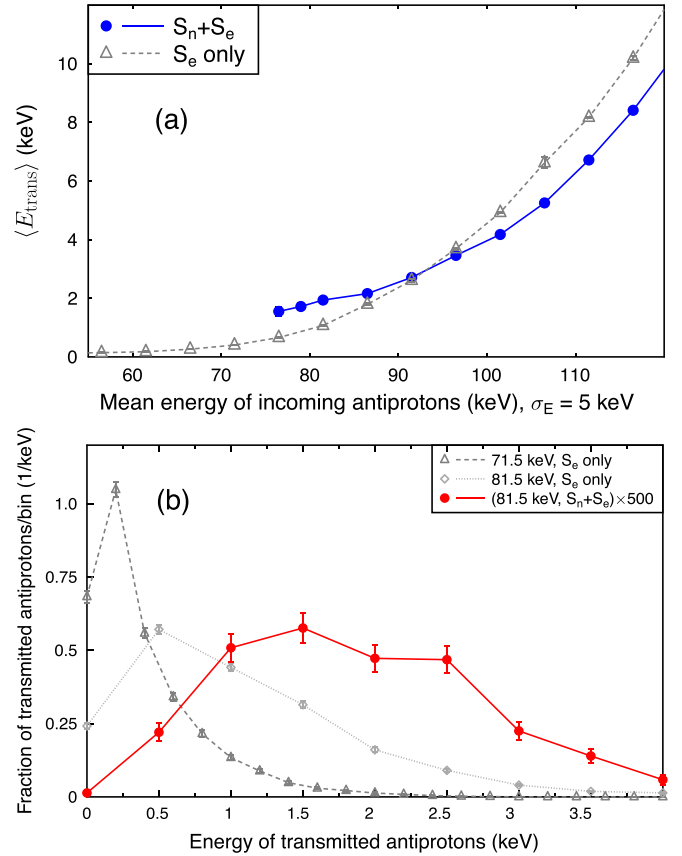


FIG. 15. (a) Average energy  $\langle E_{\text{trans}} \rangle$  of the antiprotons that emerge from the Ag-coated BoPET foil, simulated with (filled circles) and without (open triangles) the contribution of the nuclear stopping power  $S_n^{\bar{p}}$ . (b) Energy distributions  $E_{\text{trans}}$  of the emerging antiprotons for incident beam energies  $E_k = 71.5$  keV (triangles) and 81.5 keV (diamonds) calculated without the  $S_n^{\bar{p}}$  contribution. The distribution corresponding to  $E_k = 81.5$  keV (circles) that includes the  $S_n^{\bar{p}}$  contribution multiplied by a factor of 500 is shown superimposed.

$\theta_{\text{exit}} > 50^\circ$  (blue open circles) reduced the yield by another  $\approx 30\%$ , whereas removing those with Larmor radii  $r_{\text{Larmor}} > 5$  mm had a relatively small effect (black filled squares). This implied that between 15% and 30% of the incident antiprotons fit into the acceptance of a Penning trap of potential depth 5–10 kV under the experimental conditions of Refs. [90,91]. Further antiprotons are lost during the subsequent electron cooling in the trap.

Figure 12(a) compares the  $E_{\text{trans}}$  distributions for a beam of  $E_k = 111.5$  keV and  $\sigma_E = 5$  keV traversing BoPET foils of a total thickness  $t_r = 1850$  nm with 25-nm-thick metallic coatings. The fraction of antiprotons that come to rest in the uncoated foil (Table II) was  $f_{\text{stop}} \approx 13\%$ . This increased to 17%, 34%, 39%, and 54% when Al, Cu, Ag, and Au coatings of incrementally larger atomic number were applied, respectively.

The results for Ag coatings applied on either the upstream (i.e., entrance), downstream (exit), or both foil surfaces are shown in Fig. 12(b). Most of the annihilations occur in the downstream Ag layer through which keV-scale antiprotons are transmitted (Table II). In the hypothetical case in which the electronic stopping power of Ag is adjusted

TABLE III. The interaction energy between an antiproton and Cu, Ag, or Au atom calculated using Turbomole. The results of both nonrelativistic and relativistic calculations are compared for the Au case.

Distance $r$ (bohr)	Interaction energy			
	Cu (hartree)	Ag (hartree)	Au, nonrelativistic (hartree)	Au, relativistic (hartree)
0.0001	-291508.38648833550	-474940.26580643450	-807336.03379621136	-808420.13061681925
0.0002	-146508.37690470659	-239940.23235710687	-412335.95031069889	-413420.08517008071
0.0005	-59508.35241796065	-98940.15187504669	-175335.79833371995	-176420.29541588307
0.0007	-42936.91114894993	-72082.97220379818	-130192.92068154475	-131277.80078712621
0.001	-30508.32615905464	-51940.08496197249	-96335.86359198054	-97421.46500700344
0.002	-16008.32786787354	-28440.19251555596	-56837.04751262472	-57925.74187472051
0.005	-7308.72560386451	-14342.09923704072	-33146.21240693634	-34245.28667918866
0.007	-5652.12163430147	-11658.59451289787	-28640.47188096082	-29745.52939401055
0.01	-4410.38144802696	-9648.44700629965	-25268.70047621010	-26380.85066817488
0.02	-2965.61295330282	-7314.47676463869	-21361.30830037316	-22486.02582377577
0.05	-2112.53034330175	-5941.93490798830	-19067.72183993740	-20204.50467965725
0.07	-1955.42417871681	-5689.43626613219	-18650.90630308088	-19791.92134002133
0.1	-1840.64679008272	-5506.51919531918	-18352.60638631582	-19496.42261014716
0.2	-1715.62679076727	-5311.73807909679	-18037.86592366084	-19185.08545412219
0.5	-1656.06317420202	-5222.04771594475	-17898.18282732744	-19046.85016222893
0.7	-1647.78410291230	-5211.17816304953	-17883.48122363939	-19032.25847588926
1.0	-1643.42474370343	-5204.70978555750	-17875.73970068054	-19024.63050177367
1.2	-1642.34392131365	-5202.86846688449	-17873.52764269468	-19022.48743140719
1.4		-5201.86914678365	-17872.30358104002	-19021.30267979419
1.5	-1641.75553599784			
1.7	-1641.27470464369	-5201.09738470162	-17871.35553309078	-19020.36535962364
2.0	-1641.01393815872	-5200.72134362942	-17870.89823761911	-19019.88937167094
2.4	-1640.82190664246	-5200.47735090297	-17870.60110433715	-19019.56220201497
2.7	-1640.73861799048	-5200.38031981547	-17870.48213868662	-19019.42810139394
3.0	-1640.68442778878	-5200.31888296489	-17870.40693124349	-19019.34369556023
3.4	-1640.63846247687	-5200.26742068708	-17870.34411274284	-19019.27454313786
3.7	-1640.61529498963	-5200.24220817752	-17870.31339520206	-19019.24173851145
4.0	-1640.59825170174	-5200.22403790369	-17870.29129686297	-19019.21887172585
4.4	-1640.58200826146	-5200.20694614383	-17870.27055090209	-19019.19824743790
4.7	-1640.57324751888	-5200.19771706353	-17870.25939300871	-19019.18762567490
5.0	-1640.56658758792	-5200.19058136831	-17870.25086801658	-19019.17981169293
5.5	-1640.55875443201	-5200.18181485256	-17870.24075683928	-19019.17101017777
6.0	-1640.55359565539	-5200.17559103446	-17870.23396470003	-19019.16548317975
7.0	-1640.54775746996	-5200.16771627142	-17870.22557667860	-19019.15914027616
8.0	-1640.54500587156	-5200.16345273919	-17870.22095626702	-19019.15590059917
9.0	-1640.54363919437	-5200.16112865958	-17870.21832141822	-19019.15416606397
10.0	-1640.54291330433	-5200.15983587899	-17870.21674899881	-19019.15318214351
11.0	-1640.54249924987	-5200.15908053792	-17870.21577143232	-19019.15259179284
12.0	-1640.54224769456	-5200.15861169572	-17870.21514194048	-19019.15222122534
13.0	-1640.54208654925	-5200.15830489253	-17870.21472324823	-19019.15197928601
14.0	-1640.54197882723	-5200.15809624241	-17870.21443637177	-19019.15181618795
15.0	-1640.54190433458	-5200.15795013177	-17870.21423476532	-19019.15170262988
20.0	-1640.54174759705	-5200.15763470004	-17870.21379785843	-19019.15146103512
25.0	-1640.54170565339	-5200.15754842050	-17870.21367770981	-19019.15139637311
30.0	-1640.54169080843	-5200.15751717581	-17870.21363460380	-19019.15137321013
35.0	-1640.54168450372	-5200.15750394388	-17870.21361571271	-19019.15136319190
40.0	-1640.54168154486	-5200.15749720351	-17870.21360716906	-19019.15135832053
45.0	-1640.54167996884	-5200.15749393473		
50.0	-1640.54167905724	-5200.15749203100		

to be equal to that of BoPET (indicated as Ag\*), about  $f_{\text{stop}} \approx 32\%$  of the antiprotons come to rest in the foil. The fact that this fraction is so similar in the Ag-coated case (39%) shows that the loss of antiprotons is primarily caused by the nuclear scattering into large angles rather than the

electronic stopping power. This fact was verified by simulations of  $E_k = 5$  keV antiprotons traversing a 25-nm-thick Ag or Ag\* foil which showed a stopped fraction  $f_{\text{stop}} = 30\%$ , whereas for a 25-nm-thick BoPET foil the fraction was 1%.

## V. DISCUSSIONS AND CONCLUSIONS

The substantial differences between the simulation results with and without the nuclear stopping contribution may seem surprising, as the  $S_n^{\bar{p}}$  values become large only at antiproton energies below about 1 keV (see Fig. 1). This difference arises from the nuclear scattering which increases both the path length of the antiprotons,

$$R_{\text{path}} = \int_{\text{path}} |d\vec{r}|, \quad (7)$$

and the corresponding total deposited electronic energy,

$$F_{D_e} = \int_{\text{path}} S_e^{\bar{p}} |d\vec{r}|. \quad (8)$$

Table II shows the  $R_{\text{path}}$  and  $F_{D_e}$  values, the stopped fraction  $f_{\text{stop}}$ , and transmitted energy  $\langle E_{\text{trans}} \rangle$  of antiprotons with average incident energy  $E_k = 111.5$  keV and energy spread  $\sigma_E = 5$  keV traversing BoPET foils with total thicknesses of 1850 nm and various coatings. One of two models of antiproton annihilation described in Sec. III A 4 was used, namely, (1) comparing the kinetic energy of the antiproton with the local interaction potential in the material or (2) adjusting the average interaction radius to  $\langle r_A \rangle = 4.4$  fm for C atoms according to Eq. (4), or to  $\langle r_A \rangle = 10$  fm for all target elements. The transmission probabilities of antiprotons calculated by both models were similar within the statistical uncertainty of the simulations, despite the fact that model A ignores the effect of in-flight annihilations. This is because a collision involving a sufficiently small impact parameter results in such a large scattering angle  $\theta$  that the antiproton likely cannot traverse the foil even if it avoids direct in-flight annihilation. This is illustrated in Fig. 13(a) which shows the trajectories of 15 antiprotons of  $E_k = 65$  keV and  $\sigma_E = 5$  keV in a 1300-nm-thick PEN foil. Figure 13(b) shows the evolutions of the energies of four of the antiprotons as a function of the depth coordinate along the thickness of the foil. Large-angle scattering and annihilation become more likely as the antiprotons slow down, so that most of the annihilations occur in the last 200-nm-thick portion of the foil [see Fig. 13(c)].

As shown in Fig. 14(a), the path length  $R_{\text{path}}$  of the cohort of antiprotons that come to rest in the foil increases with the beam energy. It eventually becomes much longer than the foil thickness of 1300 nm in the region above the minimum incident energy  $E_k = 50$  keV that allows antiproton transmission [Fig. 14(c)].

The  $R_{\text{path}}$  values of the transmitted antiprotons [Fig. 14(b)], on the other hand, remain only slightly longer than the foil thickness regardless of the incident energy between  $E_k = 50$  and 120 keV. The deposited electronic energy  $F_{D_e}$  increases with  $E_k$ , whereas the energy  $F_{D_n}$  lost by nuclear stopping remains negligibly small. As shown in Table II, these  $R_{\text{path}}$  and  $F_{D_e}$  values vary by only  $\approx 1\%$  for foils with Al, Cu, Ag, or Au coatings, whereas the fraction of stopped antiprotons increases from  $f_{\text{stop}} = 17\%$  to 54%. All these results show that the transmitted antiprotons represent the cohort that statistically managed to traverse the foil without undergoing scattering events into large angles.

Figure 15(a) compares the average energies  $\langle E_{\text{trans}} \rangle$  of the cohort of antiprotons that were transmitted through the Ag-coated BoPET foil as a function of incident energy  $E_k$ , calculated with and without the nuclear stopping contribution. In the region  $E_k = 100$ –120 keV the nuclear stopping reduced the  $\langle E_{\text{trans}} \rangle$  value by 1–2 keV. We attempted to slow down more antiprotons to  $E_{\text{trans}} \leq 1$  keV by reducing the incident beam energy to  $E_k = 81.5$  keV. This caused most of the antiprotons to annihilate in the foil [Fig. 15(b)] because of the the rapid increase of the nuclear scattering cross section at energies below 2–3 keV (Fig. 1). Further losses are expected due to antiproton capture at sub-keV energies [51,52]. Alternative methods such as electrostatic drift tubes [166] may be used to efficiently decelerate such slow antiprotons.

In conclusion, we showed that the MD-RIA model of antiproton deceleration in polymer foils which includes the effects of nuclear stopping in antiproton-atom interaction potentials, is in good agreement with experimental results in the sub-100 keV energy region. The significant nuclear scattering predicted by this model was found to affect the transmission probability and energy distribution of the antiprotons that emerge from the foils, particularly in the energy range below 1–2 keV. Some recent experiments at ELENA have utilized foils with Ag or Au coatings of a few tens nanometer thickness to reduce the thermal radiation entering a Penning trap or the outgasing of contamination gases, but nuclear scattering in materials of such high atomic number decreases the yield of the transmitted antiprotons. A beam with a small energy spread  $\sigma_E < 1$  keV should ideally be slowed down in an uniform foil made of light atoms with a thickness adjusted with a few tens nanometer accuracy. The typical uncertainties of the order of  $\pm 100$  nm in the thickness of polymer foils may be compensated by tuning the energy of the incident beam over a range of  $\pm 10$  keV. The results will aid the design of experiments to increase the production of antihydrogen and antiprotonic atoms.

The simulation results presented in this paper, the source code of MDRANGE, and the software dpc used to create the trajectory plots are available at [167].

## ACKNOWLEDGMENTS

We thank Prof. Andrea Sand for collaboration in making an open access distribution of MDRANGE, S. S. Fabbri, N. Kuroda, N. Madsen, and L. Venturelli for valuable discussions, the ASACUSA collaboration, and the PS and AD operations staff of CERN. Grants of computer time from CSC, the Finnish IT Center for Science, as well as the Finnish Grid and Cloud Infrastructure (persistent identifier urn:nbn:fi:research-infras-2016072533) are gratefully acknowledged. The experimental work on  $\bar{p}^4\text{He}^+$  was supported by the Max-Planck-Gesellschaft.

## APPENDIX: ANTIPROTON-ATOM INTERACTION ENERGIES

The antiproton-Cu, Ag, and Au interaction energies calculated in this work are provided in Table III. The fit result for Au shown in Table I was obtained

using the interaction energies that include relativistic corrections that significantly influence the quantum-chemical

properties [168]. The nonrelativistic energies are also shown.

- 
- [1] W. H. Bragg and R. Kleeman, On the alpha particles of radium, and their loss of range in passing through various atoms and molecules, *London Edinburgh Dublin Philos. Mag. J. Sci.* **10**, 318 (1905).
- [2] N. Bohr, On the theory of the decrease of velocity of moving electrified particles on passing through matter, *London Edinburgh Dublin Philos. Mag. J. Sci.* **25**, 10 (1913).
- [3] E. Fermi and E. Teller, The capture of negative mesotrons in matter, *Phys. Rev.* **72**, 399 (1947).
- [4] J. Lindhard, M. Scharff, and H. E. Schiøtt, Range concepts and heavy ion ranges, *Kgl. Danske Vid. Selskab, Mat.-Fys. Medd.* **33**, 1 (1963).
- [5] R. Smith (ed.), *Atomic & Ion Collisions in Solids and at Surfaces: Theory, Simulation and Applications* (Cambridge University Press, Cambridge, 1997).
- [6] G. S. Was, *Fundamentals of Radiation Materials Science* (Springer, Berlin, 2017).
- [7] J. F. Ziegler, J. P. Biersack, and U. Littmark, *The Stopping and Range of Ions in Matter* (Pergamon, New York, 1985).
- [8] J. F. Ziegler, J. P. Biersack, and M. D. Ziegler, *SRIM—The Stopping and Range of Ions in Matter* (SRIM Co., Chester, MD, 2008).
- [9] A. A. Correa, J. Kohanoff, E. Artacho, D. Sánchez-Portal, and A. Caro, Nonadiabatic Forces in Ion-Solid Interactions: The Initial Stages of Radiation Damage, *Phys. Rev. Lett.* **108**, 213201 (2012).
- [10] M. Caro, A. Correa, E. Artacho, and A. Caro, Stopping power beyond the adiabatic approximation, *Sci. Rep.* **7**, 2618 (2017).
- [11] M. Backman, F. Djurabekova, O. H. Pakarinen, K. Nordlund, Y. Zhang, M. Toulemonde, and W. J. Weber, Cooperative effect of electronic and nuclear stopping of ion irradiation damage in silica, *J. Phys. D: Appl. Phys.* **45**, 505305 (2012).
- [12] L. Thomé, A. Debelle, F. Garrido, S. Mylonas, B. Décamps, C. Bachelet, G. Sattonnay, S. Moll, S. Pellegrino, S. Miro, P. Trocellier *et al.*, Radiation effects in nuclear materials: Role of nuclear and electronic energy losses and their synergy, *Nucl. Instrum. Methods Phys. Res. B* **307**, 43 (2013).
- [13] W. J. Weber, E. Zarkadoula, O. H. Pakarinen, R. Sachan, M. F. Chisholm, P. Liu, H. Xue, K. Jin, and Y. Zhang, Synergy of elastic and inelastic energy loss on ion track formation in SrTiO<sub>3</sub>, *Sci. Rep.* **5**, 7726 (2015).
- [14] L. H. Andersen, P. Hvelplund, H. Knudsen, S. P. Møller, J. O. P. Pedersen, E. Uggerhøj, K. Elsener, and E. Morenzoni, Measurement of the  $Z_1^3$  Contribution to the Stopping Power using MeV Protons and Antiprotons: The Barkas Effect, *Phys. Rev. Lett.* **62**, 1731 (1989).
- [15] H. H. Mikkelsen and P. Sigmund, Barkas effect in electronic stopping power: Rigorous evaluation for the harmonic oscillator, *Phys. Rev. A* **40**, 101 (1989).
- [16] G. Gabrielse, X. Fei, L. A. Orozco, S. L. Rolston, R. L. Tjoelker, T. A. Trainor, J. Haas, H. Kalinowsky, and W. Kells, Barkas effect with use of antiprotons and protons, *Phys. Rev. A* **40**, 481 (1989).
- [17] R. Medenwaldt, S. Møller, E. Uggerhøj, T. Worm, P. Hvelplund, H. Knudsen, K. Elsener, and E. Morenzoni, Measurement of the stopping power of silicon for antiprotons between 0.2 and 3 MeV, *Nucl. Instrum. Methods Phys. Res. B* **58**, 1 (1991).
- [18] A. Adamo *et al.*, Antiproton stopping power in hydrogen below 120 keV and the Barkas effect, *Phys. Rev. A* **47**, 4517 (1993).
- [19] S. T. Nakagawa, The electronic stopping power of channeled antiproton, *Radiat. Eff. Defects Solids* **140**, 75 (1996).
- [20] S. P. Møller, E. Uggerhøj, H. Bluhme, H. Knudsen, U. Mikkelsen, K. Paludan, and E. Morenzoni, Direct measurements of the stopping power for antiprotons of light and heavy targets, *Phys. Rev. A* **56**, 2930 (1997).
- [21] S. P. Møller, A. Csete, T. Ichioka, H. Knudsen, U. I. Uggerhøj, and H. H. Andersen, Antiproton Stopping at Low Energies: Confirmation of Velocity-Proportional Stopping Power, *Phys. Rev. Lett.* **88**, 193201 (2002).
- [22] S. P. Møller, A. Csete, T. Ichioka, H. Knudsen, U. I. Uggerhøj, and H. H. Andersen, Stopping Power in Insulators and Metals without Charge Exchange, *Phys. Rev. Lett.* **93**, 042502 (2004).
- [23] S. P. Møller, A. Csete, T. Ichioka, H. Knudsen, H.-P. E. Kristiansen, U. I. Uggerhøj, H. H. Andersen, P. Sigmund, and A. Schinner, Antiproton and proton energy loss straggling at keV energies, *Eur. Phys. J. D* **46**, 89 (2008).
- [24] N. R. Arista and A. F. Lifschitz, Nonlinear calculation of stopping powers for protons and antiprotons in solids: The Barkas effect, *Phys. Rev. A* **59**, 2719 (1999).
- [25] P. Sigmund and A. Schinner, Binary theory of antiproton stopping, *Eur. Phys. J. D* **15**, 165 (2001).
- [26] E. Lodi Rizzini, A. Bianconi, M. P. Bussa, M. Corradini, A. Donzella, L. Venturelli, M. Bargiotti, A. Bertin, M. Bruschi, M. Capponi *et al.*, Barkas Effect for Antiproton Stopping in H<sub>2</sub>, *Phys. Rev. Lett.* **89**, 183201 (2002).
- [27] U. I. Uggerhøj, H. Bluhme, H. Knudsen, S. P. Møller, E. Uggerhøj, E. Morenzoni, and C. Scheidenberger, Channeling of antiprotons, *Nucl. Instrum. Methods Phys. Res. B* **207**, 402 (2003).
- [28] P. L. Grande and G. Schiwietz, Improved calculations of the electronic and nuclear energy loss for light ions penetrating H and He targets, *Braz. J. Phys.* **24**, 551 (1994).
- [29] P. L. Grande and G. Schiwietz, Ionization and energy loss beyond perturbation theory, *Adv. Quantum Chem.* **45**, 7 (2004).
- [30] R. Cabrera-Trujillo, J. R. Sabin, Y. Öhrn, and E. Deumens, Stopping of swift antiprotons by hydrogen atoms and the Barkas correction, *Phys. Rev. A* **71**, 012901 (2005).
- [31] A. Lühr and A. Saenz, Stopping power of antiprotons in H, H<sub>2</sub>, and He targets, *Phys. Rev. A* **79**, 042901 (2009).
- [32] S. Borbély, X.-M. Tong, S. Nagele, J. Feist, I. Březinová, F. Lackner, L. Nagy, K. Tókési, and J. Burgdörfer, Electron correlations in the antiproton energy-loss distribution in He, *Phys. Rev. A* **98**, 012707 (2018).
- [33] J. J. Bailey, A. S. Kadyrov, I. B. Abdurakhmanov, D. V. Fursa, and I. Bray, Antiproton stopping in atomic targets, *Phys. Rev. A* **92**, 022707 (2015).

- [34] J. J. Bailey, A. S. Kadyrov, I. B. Abdurakhmanov, D. V. Fursa, and I. Bray, Antiproton stopping in  $H_2$  and  $H_2O$ , *Phys. Rev. A* **92**, 052711 (2015).
- [35] C. C. Montanari and J. E. Miraglia, Low- and intermediate-energy stopping power of protons and antiprotons in solid targets, *Phys. Rev. A* **96**, 012707 (2017).
- [36] H. J. Lüdde, M. Horbatsch, and T. Kirchner, Calculation of energy loss in antiproton collisions with many-electron systems using Ehrenfest's theorem, *Phys. Rev. A* **104**, 032813 (2021).
- [37] J. M. Pruneda, D. Sánchez-Portal, A. Arnau, J. I. Juaristi, and E. Artacho, Electronic Stopping Power in LiF from First Principles, *Phys. Rev. Lett.* **99**, 235501 (2007).
- [38] M. H. Holzschneider *et al.*, The biological effectiveness of antiproton irradiation, *Radiother. Oncol.* **81**, 233 (2006).
- [39] S. Chauvie, P. Nieminen, and M. G. Pia, Geant4 model for the stopping power of low energy negatively charged hadrons, *IEEE Trans. Nucl. Sci.* **54**, 578 (2007).
- [40] M. Quijada, A. G. Borisov, I. Nagy, R. Díez Muiño, and P. M. Echenique, Time-dependent density-functional calculation of the stopping power for protons and antiprotons in metals, *Phys. Rev. A* **75**, 042902 (2007).
- [41] W. H. Barkas, J. N. Dyer, and H. H. Heckman, Resolution of the  $\Sigma^-$ -Mass Anomaly, *Phys. Rev. Lett.* **11**, 26 (1963).
- [42] P. Sigmund and A. Schinner, Anatomy of the Barkas effect, *Nucl. Instrum. Methods Phys. Res. B* **212**, 110 (2003).
- [43] H. Knudsen, H. P. E. Kristiansen, H. D. Thomsen, U. I. Uggerhoj, T. Ichioka, S. P. Moller, C. A. Hunniford, R. W. McCullough, M. Charlton, N. Kuroda *et al.*, Ionization of Helium and Argon by Very Slow Antiproton Impact, *Phys. Rev. Lett.* **101**, 043201 (2008).
- [44] H. Knudsen, H. A. Torii, M. Charlton, Y. Enomoto, I. Georgescu, C. A. Hunniford, C. H. Kim, Y. Kanai, H. P. E. Kristiansen, N. Kuroda *et al.*, Target Structure Induced Suppression of the Ionization Cross Section for Very Low Energy Antiproton-Hydrogen Collisions, *Phys. Rev. Lett.* **105**, 213201 (2010).
- [45] T. Kirchner and H. Knudsen, Current status of antiproton impact ionization of atoms and molecules: Theoretical and experimental perspectives, *J. Phys. B* **44**, 122001 (2011).
- [46] M. Agnello *et al.*, Antiproton Slowing Down in  $H_2$  and He and Evidence of Nuclear Stopping Power, *Phys. Rev. Lett.* **74**, 371 (1995).
- [47] G. Schiwietz, U. Wille, R. D. Muino, P. Fainstein, and P. Grande, Comprehensive analysis of the stopping power of antiprotons and negative muons in He and  $H_2$  gas targets, *J. Phys. B* **29**, 307 (1996).
- [48] K. Nordlund, D. Sundholm, P. Pyykkö, D. M. Zambrano, and F. Djurabekova, Nuclear stopping power of antiprotons, *Phys. Rev. A* **96**, 042717 (2017).
- [49] A. Bertin *et al.*, Experimental antiproton nuclear stopping power in  $H_2$  and  $D_2$ , *Phys. Rev. A* **54**, 5441 (1996).
- [50] A. Bianconi, M. Corradini, A. Cristiano, M. Leali, E. Lodi Rizzini, L. Venturelli, N. Zurlo, and R. Donà, Experimental evidence of antiproton reflection by a solid surface, *Phys. Rev. A* **78**, 022506 (2008).
- [51] J. S. Cohen, Molecular effects on antiproton capture by  $H_2$  and the states of  $\bar{p}p$  formed, *Phys. Rev. A* **56**, 3583 (1997).
- [52] J. S. Cohen, Multielectron effects in capture of antiprotons and muons by helium and neon, *Phys. Rev. A* **62**, 022512 (2000).
- [53] J. S. Cohen, Capture of negative exotic particles by atoms, ions and molecules, *Rep. Prog. Phys.* **67**, 1769 (2004).
- [54] K. Tökési, B. Juhász, and J. Burgdörfer, Exotic Rydberg atom formation in low-energy antiproton-helium collisions, *J. Phys. B* **38**, S401 (2005).
- [55] J. Révai and N. Shevchenko, Capture of slow antiprotons by helium atoms, *Eur. Phys. J. D* **37**, 83 (2006).
- [56] X. M. Tong, K. Hino, and N. Toshima, Anomalous Bumpy Structures in the Capture Cross Sections of Antiprotons by Helium, *Phys. Rev. Lett.* **101**, 163201 (2008).
- [57] K. Sakimoto, Formation of antiprotonic helium  $\bar{p}He^+$  and ionization in low-energy collisions of  $\bar{p}$  with He in the ground  $1^1S$  and metastable  $2^3S$  and  $2^1S$  states, *Phys. Rev. A* **91**, 042502 (2015).
- [58] M. Hori, J. Eades, R. S. Hayano, T. Ishikawa, J. Sakaguchi, T. Tasaki, E. Widmann, H. Yamaguchi, H. A. Torii, B. Juhász *et al.*, Primary Populations of Metastable Antiprotonic  $^4He$  and  $^3He$  Atoms, *Phys. Rev. Lett.* **89**, 093401 (2002).
- [59] Brückner *et al.*, Measurements of the antiproton-proton annihilation cross-section in the beam momentum range between 180 and 600 MeV/c, *Z. Phys. A* **335**, 217 (1990).
- [60] A. Bertin *et al.*,  $\bar{p}p$  annihilation cross section at very low energy, *Phys. Lett. B* **369**, 77 (1996).
- [61] A. Benedettini *et al.*,  $\bar{p}p$  partial cross sections at low energy, *Nucl. Phys. B, Proc. Suppl.* **56**, 58 (1997).
- [62] A. Zenoni *et al.*, New measurements of the  $\bar{p}p$  annihilation cross section at very low energy, *Phys. Lett. B* **461**, 405 (1999).
- [63] R. Bizzarri, P. Guidoni, F. Marcelja, F. Marzano, E. Castelli, and M. Sessa, Antiproton-deuteron low-energy cross-sections, *Nuovo Cimento A* **22**, 225 (1974).
- [64] T. Kalogeropoulos and G. S. Tzanakos, Total and partial  $\bar{p}d$  cross sections from 0.26 to 0.47 GeV/c, *Phys. Rev. D* **22**, 2585 (1980).
- [65] A. Zenoni *et al.*,  $\bar{p}D$  and  $\bar{p}^4He$  annihilation cross sections at very low energy, *Phys. Lett. B* **461**, 413 (1999).
- [66] A. Bianconi *et al.*, Measurement of the antiproton-nucleus annihilation cross section at 5.3 MeV, *Phys. Lett. B* **704**, 461 (2011).
- [67] H. Aghai-Khozani *et al.*, First experimental detection of antiproton in-flight annihilation on nuclei at  $\sim 130$  keV, *Eur. Phys. J. Plus* **127**, 125 (2012).
- [68] H. Aghai-Khozani *et al.*, Measurement of the antiproton-nucleus annihilation cross-section at low energy, *Nucl. Phys. A* **970**, 366 (2018).
- [69] H. Aghai-Khozani *et al.*, Limits on antiproton-nuclei annihilation cross sections at  $\sim 125$  keV, *Nucl. Phys. A* **1009**, 122170 (2021).
- [70] K. Nakamura, J. Chiba, T. Fujii, H. Iwasaki, T. Kageyama, S. Kuribayashi, T. Sumiyoshi, T. Takeda, H. Ikeda, and Y. Takada, Absorption and Forward Scattering of Antiprotons by C, Al, and Cu Nuclei in the Region 470–880 MeV/c, *Phys. Rev. Lett.* **52**, 731 (1984).
- [71] F. Balestra *et al.*, Low-energy antiproton-neon interaction, *Nucl. Phys. A* **452**, 573 (1986).
- [72] A. Bianconi *et al.*, Antiproton-neon annihilation at 57 MeV/c, *Phys. Lett. B* **481**, 194 (2000).
- [73] V. Ashford, M. E. Sainio, M. Sakitt, J. Skelly, R. Debbe, W. Fickinger, R. Marino, and D. K. Robinson, Low energy antiproton nuclear absorption cross sections, *Phys. Rev. C* **31**, 663 (1985).

- [74] A. Bianconi, G. Bonomi, E. Lodi Rizzini, L. Venturelli, and A. Zenoni, Coulomb corrections to low energy antiproton annihilation cross sections on protons and nuclei, *Phys. Rev. C* **62**, 014611 (2000).
- [75] A. Gal, E. Friedman, and C. Batty, Saturation of low-energy antiproton annihilation on nuclei, *Phys. Lett. B* **491**, 219 (2000).
- [76] C. J. Batty, E. Friedman, and A. Gal, Unified optical-model approach to low-energy antiproton annihilation on nuclei and to antiprotonic atoms, *Nucl. Phys. A* **689**, 721 (2001).
- [77] M. P. Allen and D. J. Tildesley, *Computer Simulation of Liquids* (Oxford University Press, Oxford, 1989).
- [78] K. Nordlund, Molecular dynamics simulation of ion ranges in the 1–100 keV energy range, *Comput. Mater. Sci.* **3**, 448 (1995).
- [79] G. Hobler and G. Betz, On the useful range of application of molecular dynamics simulations in the recoil interaction approximation, *Nucl. Instrum. Methods Phys. Res. B* **180**, 203 (2001).
- [80] K. Nordlund, F. Djurabekova, and G. Hobler, Large fraction of crystal directions leads to ion channeling, *Phys. Rev. B* **94**, 214109 (2016).
- [81] K. Nordlund, Slowing down of antiprotons in Al foils, *Results Phys.* **8**, 683 (2018).
- [82] Each simulation carried out on a processor with a calculation speed of  $\approx 10^{10}$  floating point operations per second took from a few days to a few weeks.
- [83] V. Chohan *et al.*, Extra Low ENergy antiproton (ELENA) ring and its transfer lines: Design report, CERN-2014-002, CERN, Geneva, Switzerland (2014).
- [84] D. Gamba *et al.*, ELENA commissioning, in *Proceedings of North American Particle Accelerator Conference NAPAC2019, Lansing MI, USA*, edited by Y. Yamazaki, T. Raubenheimer, A. McCausey, and V. RW Schaa (JACoW Publishing, Geneva, Switzerland, 2019), p. WEYBB1.
- [85] M. Ahmadi *et al.*, Investigation of the fine structure of antihydrogen, *Nature (London)* **578**, 375 (2020).
- [86] C. J. Baker *et al.*, Laser cooling of antihydrogen atoms, *Nature (London)* **592**, 35 (2021).
- [87] S. Aghion *et al.*, Compression of a mixed antiproton and electron non-neutral plasma to high densities, *Eur. Phys. J. D* **72**, 76 (2018).
- [88] P. Perez *et al.*, The GBAR antimatter gravity experiment, *Hyperfine Interact.* **233**, 21 (2015).
- [89] G. Gabrielse, R. Kalra, W. S. Kolthammer, R. McConnell, P. Richerme, D. Grzonka, W. Oelert, T. Seifzick, M. Zielinski, D. W. Fitzakerley *et al.*, Trapped Antihydrogen in Its Ground State, *Phys. Rev. Lett.* **108**, 113002 (2012).
- [90] N. Kuroda, H. A. Torii, K. Yoshiki Franzen, Z. Wang, S. Yoneda, M. Inoue, M. Hori, B. Juhasz, D. Horvath, H. Higaki *et al.*, Confinement of a Large Number of Antiprotons and Production of an Ultraslow Antiproton Beam, *Phys. Rev. Lett.* **94**, 023401 (2005).
- [91] N. Kuroda, H. A. Torii, Y. Nagata, M. Shibata, Y. Enomoto, H. Imao, Y. Kanai, M. Hori, H. Saitoh, H. Higaki *et al.*, Development of a monoenergetic ultraslow antiproton beam source for high-precision investigation, *Phys. Rev. ST Accel. Beams* **15**, 024702 (2012).
- [92] S. Fabbri and W. Bertsche, Optimization of antiproton capture for antihydrogen creation in the ALPHA experiment, in *8th International Beam Instrumentation Conference (JACoW Publishing, Geneva, Switzerland, 2019)*, pp. 637–641.
- [93] V. I. Korobov, L. Hilico, and J.-P. Karr,  $m\alpha^7$ -Order Corrections in the Hydrogen Molecular Ions and Antiprotonic Helium, *Phys. Rev. Lett.* **112**, 103003 (2014).
- [94] V. I. Korobov, Bethe logarithm for resonant states: Antiprotonic helium, *Phys. Rev. A* **89**, 014501 (2014).
- [95] M. Hori *et al.*, Two-photon laser spectroscopy of antiprotonic helium and the antiproton-to-electron mass ratio, *Nature (London)* **475**, 484 (2011).
- [96] M. Hori *et al.*, Buffer-gas cooling of antiprotonic helium to 1.5 to 1.7 K, and antiproton-to-electron mass ratio, *Science* **354**, 610 (2016).
- [97] F. Ficek, P. Fadeev, V. V. Flambaum, D. F. Jackson Kimball, M. G. Kozlov, Y. V. Stadnik, and D. Budker, Constraints on Exotic Spin-Dependent Interactions between Matter and Antimatter from Antiprotonic Helium Spectroscopy, *Phys. Rev. Lett.* **120**, 183002 (2018).
- [98] D. Baye, J. Dohet-Eraly, and P. Schoofs, Structure changes along the lowest rotational band of the antiprotonic helium atom, *Phys. Rev. A* **99**, 022508 (2019).
- [99] M. Germann, S. Patra, J. P. Karr, L. Hilico, V. I. Korobov, E. J. Salumbides, K. S. E. Eikema, W. Ubachs, and J. C. J. Koelemeij, Three-body QED test and fifth-force constraint from vibrations and rotations of  $\text{HD}^+$ , *Phys. Rev. Research* **3**, L022028 (2021).
- [100] J. DiSciaccia, M. Marshall, K. Marable, G. Gabrielse, S. Ettenauer, E. Tardiff, R. Kalra, D. W. Fitzakerley, M. C. George, E. A. Hessels *et al.*, One-Particle Measurement of the Antiproton Magnetic Moment, *Phys. Rev. Lett.* **110**, 130801 (2013).
- [101] M. Borchert *et al.*, A 16-parts-per-trillion measurement of the antiproton-to-proton charge–mass ratio, *Nature (London)* **601**, 53 (2022).
- [102] C. Smorra *et al.*, A parts-per-billion measurement of the antiproton magnetic moment, *Nature (London)* **550**, 371 (2017).
- [103] D. Bakalov, B. Jeziorski, T. Korona, K. Szalewicz, and E. Tchukova, Density Shift and Broadening of Transition Lines in Antiprotonic Helium, *Phys. Rev. Lett.* **84**, 2350 (2000).
- [104] B. Obreshkov and D. Bakalov, Collisional shift and broadening of the transition lines in pionic helium, *Phys. Rev. A* **93**, 062505 (2016).
- [105] M. Hori, J. Eades, R. S. Hayano, T. Ishikawa, J. Sakaguchi, E. Widmann, H. Yamaguchi, H. A. Torii, B. Juhasz, D. Horvath, and T. Yamazaki, Sub-ppm Laser Spectroscopy of Antiprotonic Helium and a CPT-Violation Limit on the Antiprotonic Charge and Mass, *Phys. Rev. Lett.* **87**, 093401 (2001).
- [106] M. Hori, H. Aghai-Khozani, A. Sótér, A. Dax, and D. Barna, Laser spectroscopy of pionic helium atoms, *Nature (London)* **581**, 37 (2020).
- [107] A. Sótér, H. Aghai-Khozani, D. Barna, A. Dax, L. Venturelli, and M. Hori, High-resolution laser resonances of antiprotonic helium in superfluid  $^4\text{He}$ , *Nature (London)* **603**, 411 (2022).
- [108] N. Paul, G. Bian, T. Azuma, S. Okada, and P. Indelicato, Testing Quantum Electrodynamics with Exotic Atoms, *Phys. Rev. Lett.* **126**, 173001 (2021).
- [109] B. D. Obreshkov, D. D. Bakalov, B. Lepetit, and K. Szalewicz, Collisional quenching of antiprotonic helium atoms in gaseous helium, *Phys. Rev. A* **69**, 042701 (2004).

- [110] V. I. Korobov, Z.-X. Zhong, and Q.-L. Tian, Leading term of the He- $\bar{p}$ He<sup>+</sup> long-range interaction, *Phys. Rev. A* **92**, 052517 (2015).
- [111] S. Maury, The antiproton decelerator: AD, *Hyperfine Interact.* **109**, 43 (1997).
- [112] T. Eriksson *et al.*, Upgrades and consolidation of the CERN AD for operation during the next decades, in *Proceedings of the Fourth International Particle Accelerator Conference, IPAC-2013, Shanghai, China*, edited by Z. Dai, C. Petit-Jean-Genaz, V. R. W. Schaa, and C. Zhang (JACoW Publishing, Geneva, Switzerland, 2013), pp. 2654–2656.
- [113] M. Hori and J. Walz, Physics at CERN’s Antiproton Decelerator, *Prog. Part. Nucl. Phys.* **72**, 206 (2013).
- [114] E. Bonderup and P. Hvelplund, Stopping power and energy straggling for swift protons, *Phys. Rev. A* **4**, 562 (1971).
- [115] A. Luukkainen and M. Hautala, Calculation of H<sup>+</sup>-ranges and H<sup>+</sup>-range straggling in the energy region 1–1000 keV, *Radiat. Eff.* **59**, 113 (1982).
- [116] M. Hautala, J. Keinonen, H. J. Whitlow, P. Tikkanen, M. Uhrmacher, and K. Lieb, Range profiles of 25–250 keV hydrogen in silicon, *Phys. Lett. A* **109**, 344 (1985).
- [117] A. Lombardi, W. Pirkel, and Y. Bylinsky, First operating experience with the CERN decelerating RFQ for antiprotons, in *PACS2001, Proceedings of the 2001 Particle Accelerator Conference*, Vol. 1 (IEEE, Chicago, Illinois, USA, 2001), pp. 585–587.
- [118] M. Hori, J. Eades, R. S. Hayano, T. Ishikawa, W. Pirkel, E. Widmann, H. Yamaguchi, H. A. Torii, B. Juhasz, D. Horvath, and T. Yamazaki, Direct Measurement of Transition Frequencies in Isolated  $\bar{p}$ He<sup>+</sup> Atoms, and New CPT-Violation Limits on the Antiproton Charge and Mass, *Phys. Rev. Lett.* **91**, 123401 (2003).
- [119] M. Hori, A. Dax, J. Eades, K. Gomikawa, R. S. Hayano, N. Ono, W. Pirkel, E. Widmann, H. A. Torii, B. Juhasz *et al.*, Determination of the Antiproton-to-Electron mass Ratio by Precision Laser Spectroscopy of  $\bar{p}$ He<sup>+</sup>, *Phys. Rev. Lett.* **96**, 243401 (2006).
- [120] M. Hori, Photocathode microwire monitor for nondestructive and highly sensitive spatial profile measurements of ultraviolet, x-ray, and charged particle beams, *Rev. Sci. Instrum.* **76**, 113303 (2005).
- [121] Y. Murakami, H. Aghai-Khozani, and M. Hori, Lead fluoride Cherenkov detector read out by avalanche photodiodes for measuring the intensities of pulsed antiproton beams, *Nucl. Instrum. Methods Phys. Res. A* **933**, 75 (2019).
- [122] M. Hori and A. Dax, Chirp-corrected, nanosecond Ti:sapphire laser with 6 MHz linewidth for spectroscopy of antiprotonic helium, *Opt. Lett.* **34**, 1273 (2009).
- [123] G. Reifenröther, E. Klempt, and R. Landua, Cascade of antiprotonic helium atoms, *Phys. Lett. B* **203**, 9 (1988).
- [124] G. Y. Korenman and S. N. Yudin, Neutralization of excited antiprotonic helium ion in collisions with helium atoms, *Eur. Phys. J. D* **75**, 64 (2021).
- [125] M. Hori, K. Yamashita, R. Hayano, and T. Yamazaki, Analog Cherenkov detectors used in laser spectroscopy experiments on antiprotonic helium, *Nucl. Instrum. Methods Phys. Res. A* **496**, 102 (2003).
- [126] K. Todoroki *et al.*, Instrumentation for measurement of in-flight annihilations of 130 keV antiprotons on thin target foils, *Nucl. Instrum. Methods Phys. Res. A* **835**, 110 (2016).
- [127] L. Thulliez *et al.*, Impact of material thicknesses on fission observables obtained with the FALSTAFF experimental setup, *EPJ Web Conf.* **146**, 04028 (2017).
- [128] M. Hori, Parallel plate chambers for monitoring the profiles of high-intensity pulsed antiproton beams, *Nucl. Instrum. Methods Phys. Res. A* **522**, 420 (2004).
- [129] E. Chason and P. R. Guduru, Tutorial: Understanding residual stress in polycrystalline thin films through real-time measurements and physical models, *J. Appl. Phys.* **119**, 191101 (2016).
- [130] O. S. Oen, D. K. Holmes, and M. T. Robinson, Ranges of energetic atoms in solids, *J. Appl. Phys.* **34**, 302 (1963).
- [131] M. T. Robinson and I. M. Torrens, Computer simulation of atomic-displacement cascades in solids in the binary-collision approximation, *Phys. Rev. B* **9**, 5008 (1974).
- [132] J. P. Biersack and L. G. Hagmark, A monte carlo computer program for the transport of energetic ions in amorphous targets, *Nucl. Instrum. Methods* **174**, 257 (1980).
- [133] J. F. Ziegler, SRIM-2013 software package, <http://www.srim.org>.
- [134] J. Allison *et al.*, Recent developments in GEANT4, *Nucl. Instrum. Methods Phys. Res. A* **835**, 186 (2016).
- [135] J. M. Fernández-Varea, R. Mayol, J. Baró, and F. Salvat, On the theory and simulation of multiple elastic scattering of electrons, *Nucl. Instrum. Methods Phys. Res. B* **73**, 447 (1993).
- [136] L. Urban, Multiple scattering model in GEANT4, Tech. Rep. CERN-OPEN-2002-070, CERN, Geneva, Switzerland (2002).
- [137] M. H. Mendenhall and R. A. Weller, An algorithm for computing screened Coulomb scattering in GEANT4, *Nucl. Instrum. Methods Phys. Res. B* **227**, 420 (2005).
- [138] V. N. Ivanchenko, O. Kadri, M. Maire, and L. Urban, Geant4 models for simulation of multiple scattering, *J. Phys.: Conf. Ser.* **219**, 032045 (2010).
- [139] V. N. Ivanchenko *et al.*, Geant4 electromagnetic physics: improving simulation performance and accuracy, in *Proceedings of the Joint International Conference on Supercomputing in Nuclear Applications and Monte Carlo SNA+MC 2013*, edited by D. Caruge, C. Calvin, C. M. Diop, F. Malvagi, and J.-C. Trama (EDP Sciences, Courtaboeuf, France, 2013).
- [140] V. Ivanchenko *et al.*, Progress of Geant4 electromagnetic physics developments and applications, *EPJ Web Conf.* **214**, 02046 (2019).
- [141] A. V. Butkevich, R. P. Kokoulin, G. V. Matushko, and S. P. Mikheyev, Comments on multiple scattering of high-energy muons in thick layers, *Nucl. Instrum. Methods Phys. Res. A* **488**, 282 (2002).
- [142] G. Wentzel, Zwei Bemerkungen über die Zerstreuung korpuskularer Strahlen als Beugungerscheinung, *Z. Phys.* **40**, 590 (1926).
- [143] P. Sigmund and U. Haagerup, Bethe stopping theory for a harmonic oscillator and Bohr’s oscillator model of atomic stopping, *Phys. Rev. A* **34**, 892 (1986).
- [144] H. H. Mikkelsen, A. Meibom, and P. Sigmund, Intercomparison of atomic models for computing stopping parameters from the Bethe theory: Atomic hydrogen, *Phys. Rev. A* **46**, 7012 (1992).
- [145] P. Sigmund, Light-ion stopping near the maximum, *Nucl. Instrum. Methods Phys. Res. B* **85**, 541 (1994).
- [146] A. R. Leach, *Molecular Modelling: Principles and Applications*, 2nd ed. (Pearson Education, Harlow, England, 2001).

- [147] K. M. Beardmore and N. Grønbech-Jensen, Efficient molecular dynamics scheme for the calculation of dopant profiles due to ion implantation, *Phys. Rev. E* **57**, 7278 (1998).
- [148] K. Nordlund, Historical review of computer simulation of radiation effects in materials, *J. Nucl. Mater.* **520**, 273 (2019).
- [149] F. Furche, R. Ahlrichs, C. Hättig, W. Klopper, M. Sierka, and F. Weigend, Turbomole, *WIREs Comput. Mol. Sci.* **4**, 91 (2014).
- [150] R. Ahlrichs, M. Bär, M. Häser, H. Horn, and C. Kölmel, Electronic structure calculations on workstation computers: The program system turbomole, *Chem. Phys. Lett.* **162**, 165 (1989).
- [151] S. G. Balasubramani *et al.*, TURBOMOLE: Modular program suite for ab initio quantum-chemical and condensed-matter simulations, *J. Chem. Phys.* **152**, 184107 (2020).
- [152] J.-D. Chai and M. Head-Gordon, Long-range corrected hybrid density functionals with damped atom-atom dispersion corrections, *Phys. Chem. Chem. Phys.* **10**, 6615 (2008).
- [153] O. Treutler and R. Ahlrichs, Efficient molecular numerical integration schemes, *J. Chem. Phys.* **102**, 346 (1995).
- [154] F. Weigend and R. Ahlrichs, Balanced basis sets of split valence, triple zeta valence and quadruple zeta valence quality for H to Rn: Design and assessment of accuracy, *Phys. Chem. Chem. Phys.* **7**, 3297 (2005).
- [155] A. Baldes and F. Weigend, Efficient two-component self-consistent field procedures and gradients: Implementation in TURBOMOLE and application to Au<sub>20</sub><sup>-</sup>, *Mol. Phys.* **111**, 2617 (2013).
- [156] Y. J. Franzke, L. Spiske, P. Pollak, and F. Weigend, Segmented contracted error-consistent basis sets of quadruple-zeta valence quality for one- and two-component relativistic all-electron calculations, *J. Chem. Theory Comput.* **16**, 5658 (2020).
- [157] C. J. Batty, E. Friedman, and J. Lichtenstadt, Optical potentials for low energy antiproton-nucleus interactions, *Phys. Lett. B* **142**, 241 (1984).
- [158] K. Protasov, G. Bonomi, E. Lodi Rizzini, and A. Zenoni, Antiproton annihilation on light nuclei at very low energies, *Eur. Phys. J. A* **7**, 429 (2000).
- [159] E. Klempt, F. Bradamante, A. Martin, and J.-M. Richard, Antinucleon–nucleon interaction at low energy: Scattering and protonium, *Phys. Rep.* **368**, 119 (2002).
- [160] P. M. Echenique, R. M. Nieminen, and R. H. Ritchie, Density functional calculation of stopping power of an electron gas for slow ions, *Solid State Commun.* **37**, 779 (1981).
- [161] J. A. Nobel, J. R. Sabin, and S. B. Trickey, Simulation of ion implantation in Si for 0.25 keV H<sup>+</sup> under channeling conditions, *Nucl. Instrum. Methods Phys. Res. B* **99**, 632 (1995).
- [162] Open source code available at <https://gitlab.com/acclab/MDRANGE>.
- [163] E. Marenkov, V. Kurnaev, A. Lasa, and K. Nordlund, On the molecular effect in hydrogen molecular ions penetration through thin films, *Nucl. Instrum. Methods Phys. Res. B* **287**, 46 (2012).
- [164] M. Matsumoto and T. Nishimura, Mersenne twister: A 623-dimensionally equidistributed uniform pseudo-random number generator, *ACM Trans. Model. Comput. Simul.* **8**, 3 (1998).
- [165] K. Nordlund and G. Hobler, Dependence of ion channeling on relative atomic number in compounds, *Nucl. Instrum. Methods Phys. Res. B* **435**, 61 (2018).
- [166] A. Husson *et al.*, A pulsed high-voltage decelerator system to deliver low-energy antiprotons, *Nucl. Instrum. Methods Phys. Res. A* **1002**, 165245 (2021).
- [167] <https://doi.org/10.23729/beab273c-478a-4217-bfac-45b0f500bcc1>.
- [168] P. Pyykkö, Theoretical chemistry of gold, *Angew. Chem. Int. Ed.* **43**, 4412 (2004).